Transient Mountain Waves and Their Interaction with Large Scales

CHIH-CHIEH CHEN

National Center for Atmospheric Research, Boulder, Colorado

GREGORY J. HAKIM AND DALE R. DURRAN

Department of Atmospheric Sciences, University of Washington, Seattle, Washington

(Manuscript received 15 August 2006, in final form 8 November 2006)

ABSTRACT

The impact of transient mountain waves on a large-scale flow is examined through idealized numerical simulations of the passage of a time-evolving synoptic-scale jet over an isolated 3D mountain. Both the global momentum budget and the spatial flow response are examined to illustrate the impact of transient mountain waves on the large-scale flow. Additionally, aspects of the spatial response are quantified by potential vorticity inversion.

Nearly linear cases exhibit a weak loss of domain-averaged absolute momentum despite the absence of wave breaking. This transient effect occurs because, over the time period of the large-scale flow, the momentum flux through the top boundary does not balance the surface pressure drag. Moreover, an adiabatic spatial redistribution of momentum is observed in these cases, which results in an increase (decrease) of zonally averaged zonal momentum south (north) of the mountain.

For highly nonlinear cases, the zonally averaged momentum field shows a region of flow deceleration downstream of the mountain, flanked by broader regions of weak flow acceleration. Cancellation between the accelerating and decelerating regions results in weak fluctuations in the volume-averaged zonal momentum, suggesting that the mountain-induced circulations are primarily redistributing momentum. Potential vorticity anomalies develop in a region of wave breaking near the mountain, and induce local regions of flow acceleration and deceleration that alter the large-scale flow.

A "perfect" conventional gravity wave–drag parameterization is implemented on a coarser domain not having a mountain, forced by the momentum flux distribution from the fully nonlinear simulation. This parameterization scheme produces a much weaker spatial response in the momentum field and it fails to produce enough flow deceleration near the 20 m s^{-1} jet. These results suggest that the potential vorticity sources attributable to the gravity wave–drag parameterization have a controlling effect on the longtime downstream influence of the mountain.

1. Introduction

It is widely recognized that disturbances generated by airflow over topography can significantly influence the atmospheric circulation. These influences fall most immediately upon locations near the topography, but over time the influence is often felt indirectly on larger scales and at remote locations due, for example, to wave propagation. As a practical matter, topographic disturbances are often unresolved by numerical models, and their indirect effects must be parameterized in terms of the larger scales. Most of what is known about the processes associated with the effect of topographic disturbances on larger scales comes from theory and idealized modeling of steady-state, uniform flows over localized obstacles. Here we break from this tradition by including dynamically consistent spatial and temporal evolution in the large-scale flows that produce the topographic disturbances and that are subsequently modified by those disturbances. Our goal is to quantify where and how such large-scale flows are affected by the topographic disturbances.

In a broad sense, the characteristics of terrain-induced perturbations depend on the strength of the incident flow and the mountain height. For example,

Corresponding author address: Chih-Chieh Chen, National Center for Atmospheric Research, P.O. Box 3000, Boulder, CO 80307-3000.
E-mail: cchen@ucar.edu

DOI: 10.1175/JAS3972.1

when the incident flow is weak or the mountain height is large, windward blocking and flow splitting is typically observed as well as lee vortex generation and lee wake formation (e.g., Smolarkiweicz and Rotunno 1989; Schär and Smith 1993a,b; Epifanio and Durran 2001, 2002a,b). If the incident flow is strong enough to overcome the topography, mountain waves are launched and they can propagate to great altitude (e.g., Queney 1948; Eliassen and Palm 1960).

In this study, we investigate the spatial response induced by breaking gravity waves in numerical simulations for fully three-dimensional dynamics. We focus on mountains sufficiently high such that persistent wave breaking takes place throughout the simulation. As noted by several previous studies (Schär and Durran 1997; Rotunno et al. 1999), potential vorticity (PV) anomalies can be generated when wave dissipation takes place. Hence, a portion of the flow response attributed to these PV anomalies can be extracted from the full response through PV inversion, defined as the balanced response, and the remaining portion may be regarded as "unbalanced." Since these PV anomalies are embedded in a dynamically consistent synoptic-scale flow, they can move far downstream of the mountain and remotely influence the flow field that they inhabit; this effect is measured here by the use of piecewise PV inversion.

The paper is organized as follows. Governing equations, numerical methods, and initial conditions are specified in section 2. Global and zonal momentum budgets for a range of mountain heights are given in section 3. Three-dimensional momentum distributions are examined in section 4 for a highly nonlinear case; the contributions to the perturbation zonal momentum field are quantified in section 5 by PV inversion. Sources for these PV anomalies are tracked in section 6. Terrain-induced perturbations in the zonally averaged zonal momentum field are examined for a range of mountain heights in section 7. A "perfect" conventional gravity wave–drag (GWD) scheme is tested in section 8, and conclusions are given in section 9.

2. Model equations and experimental design

Details of model equations and experimental setup for this study are given in section 2 of Chen et al. (2005, hereafter CDH). Here we briefly review the physical and mathematical framework considered in this study and establish notation for later reference.

We employ the compressible Boussinesq equations on an f plane as described by

$$\frac{D\mathbf{v}}{Dt} + f\mathbf{k} \times \mathbf{v} + \nabla P = g\left(\frac{\theta - \theta_r}{\theta_0}\right)k + \mathbf{F}, \tag{1}$$

$$\frac{D\theta}{Dt} = H, \tag{2}$$

$$\left(\frac{\partial}{\partial t} + u_0\frac{\partial}{\partial x}\right)P + c_{s_0}^2\nabla \cdot \mathbf{v} = 0, \tag{3}$$

where

$$\frac{D}{Dt} = \frac{\partial}{\partial t} + (u_0 + u)\frac{\partial}{\partial x} + \upsilon\frac{\partial}{\partial y} + w\frac{\partial}{\partial z}.$$

Here (x, y, z) are the spatial coordinates, $\mathbf{v}$ is the velocity vector $(u_0 + u, \upsilon, w)$, $\mathbf{k}$ is the vertical unit vector, and f is the Coriolis parameter. Symbols with subscript "0" denote constant reference values; u_0 is a constant westerly flow. The potential temperature is θ, c_{s_0} is the speed of sound, g is gravity, and $\mathbf{F}$ and H represent friction and diabatic sources, respectively, which are parameterized in terms of an eddy diffusivity K following Lilly (1962); their exact expression is given in CDH.

The pressure gradient force is expressed as the gradient of a potential associated with the pressure field in the Boussinesq approximation. Let c_p be the specific heat of air at constant pressure, R the gas constant, and define the Exner function as $\Pi = (p/p_0)^{R/c_p}$. Divide Π and θ into a vertically varying reference state and a remainder such that $\Pi = \Pi_r(z) + \Pi_g(y) + \Pi'(x, y, z, t)$ and $\theta = \theta_r(z) + \theta'(x, y, z, t)$, where the reference state (Π_r, θ_r) is in hydrostatic balance $(c_p\theta_r\partial\Pi_r/\partial z = -g)$, and Π_g is a barotropic contribution balancing the mean flow $(c_p\theta_0\partial\Pi_g/\partial y = -fu_0)$. Then the Boussinesq pressure potential in geostrophic balance with u_0 may be defined as $P_g = c_p\theta_0\Pi_g$, and the perturbation about P_g as $P = c_p\theta_0\Pi'$ (see Durran 1999, p. 24). In these simulations $\theta_0 = 288$ K.

The initial condition is a dynamically consistent synoptic-scale disturbance consisting of the superposition of a uniform westerly mean flow at speed u_0 and a barotropic square wave with horizontal velocities (u_s, υ_s), amplitude u_0, and wavelength L given by

$$u_s(x, y, z) = u_0\cos\left[\frac{2\pi(x - x_0)}{L}\right]\cos\left(\frac{2\pi y}{L}\right),$$

$$\upsilon_s(x, y, z) = u_0\sin\left[\frac{2\pi(x - x_0)}{L}\right]\sin\left(\frac{2\pi y}{L}\right).$$

The initial potential temperature field is horizontally uniform and increases with height such that the Brunt–Väisälä frequency (N) is constant:

$$N^2 = \frac{g}{\theta_0}\frac{d\theta_r}{dz} = 10^{-4}\ \mathrm{s}^{-2}.$$

The initial perturbation pressure potential P_s is obtained through a steady-state nonlinear balance inversion of the square-wave horizontal velocity field. The horizontal distribution of $P_g + P_s$ is shown in Fig. 1a. Note that the mountain is initially located in a region of stagnant flow.

In the absence of the topography, the square wave is an exact solution to the nonlinear governing Eqs. (1)–(3), which translates eastward without changing form in the mean flow at speed u_0, that is, the large-scale flow is given by

$$U = u_s(x - u_0t, y) + u_0, \quad V = v_s(x - u_0t, y),$$
$$W = 0, \quad P_{\mathrm{LS}} = P_s(x - u_0t, y). \tag{4}$$

In this study, $u_0 = 10\ \mathrm{m\ s^{-1}}$ and $L = 1800$ km, implying that all synoptic-scale fields are periodic with a period τ of 50 h. In particular, as shown in Fig. 1b, the synoptic-scale cross-mountain wind speed over the ridge crest rises from 0 to 20 $\mathrm{m\ s^{-1}}$ and then returns to 0 as t increases from 0 to τ.

The isolated ridge is centered in the region of initially stagnant flow at $(x, y) = (x_0, L/2)$. As in Epifanio and Durran (2001) and CDH, it is given by

$$h_s(x, y) = \begin{cases} \dfrac{h}{16}\left[1 + \cos\left(\dfrac{\pi r}{4a}\right)\right]^4, & \text{if} \quad r \le 4a; \\ 0, & \text{otherwise,} \end{cases}$$

where

$$r^2 = \begin{cases} (x - x_0)^2 + [|y - L/2| - (\beta - 1)a]^2, & \text{if} \quad |y - L/2| > (\beta - 1)a; \\ (x - x_0)^2, & \text{otherwise.} \end{cases}$$

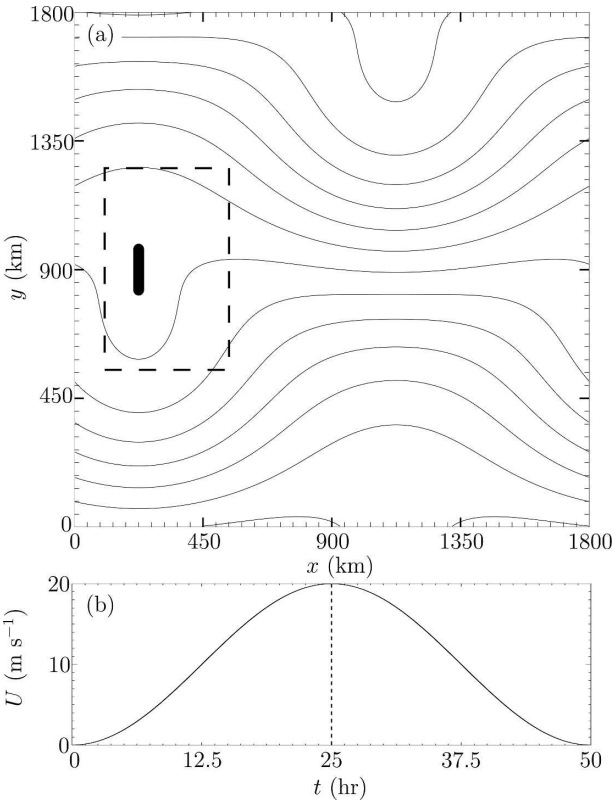

FIG. 1. (a) The isolated ridge (shown in black) in relation to the initial synoptic-scale flow shown by isolines of $P_g + P_s$ (contour interval of 150 $\mathrm{m^2\ s^{-2}}$). The dashed rectangle shows the location of the nested fine grid described in section 4. (b) The synoptic-scale zonal flow as a function of time at the crest of the mountain.

The approximate half-width at half-height is $a = 18$ km; the y–x aspect ratio is $\beta = 5$, $x_0 = 225$ km, and the ridge maximum ridge height h_0 varies between 12.5 and 1500 m in these simulations.

The computational domain is doubly periodic over a distance of $L = 1800$ km in both x and y, with a horizontal grid spacing of 6 km unless otherwise specified. The physically relevant portion of the computational domain is 16 km deep. This layer is topped by a 16-km-deep wave-absorbing layer with Rayleigh damping applied to perturbations of small scales such that the large-scale flow is unchanged. The lower boundary condition is free slip along the topography.

3. Global and zonal momentum budgets

In an earlier study, CDH demonstrate that the characteristics of transient mountain waves embedded in an evolving synoptic-scale flow can greatly deviate from those of the steady-state solution. One surprising result presented by CDH is that due to wave packet accumulation, the momentum flux in the mid- and upper troposphere tends to be strongest when the mean flow is increasing. This feature, which would not have been anticipated under the current GWD parameterizations, imposes a surprising zonal mean flow acceleration in the lower troposphere. Here we extend this research by examining the influence of the waves on the domain-averaged flow and the zonal-mean momentum field for mountain heights ranging from 12.5 to 1500 m.

Figure 2 shows the evolution of the normalized pressure drag across mountains of different heights. The quantity plotted in Fig. 2 is $\mathcal{D}'$, the mesoscale component[1] of

[1] The component of the pressure drag due to the square wave is removed.

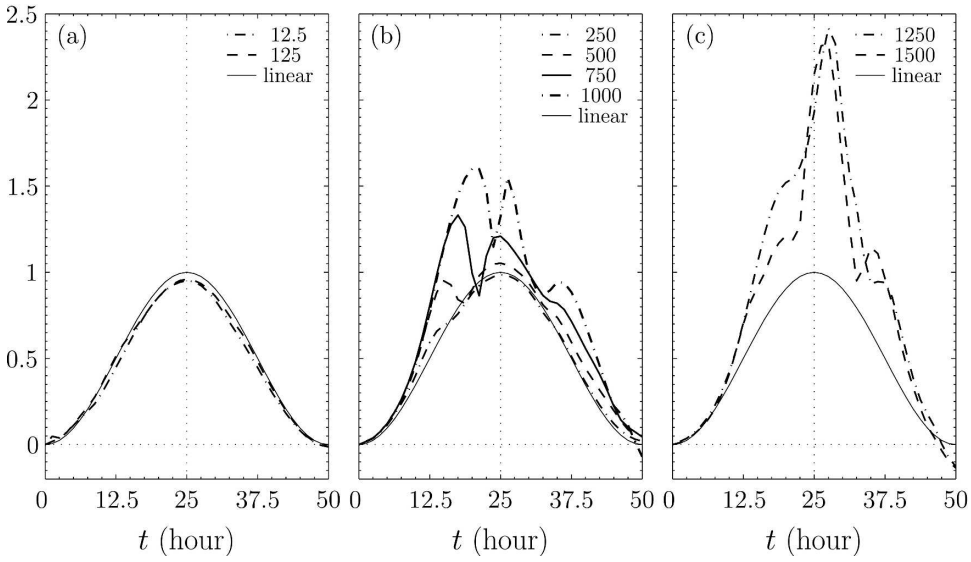

FIG. 2. Time evolution of normalized mesoscale pressure drag ($\mathcal{D}'$). The normalization is done by dividing each value by the pressure drag for the linear steady-state solution for a uniform 20 m s^{-1} flow over the same 3D ridge: (a) the quasi-linear regime with drags for mountain heights of 12.5 and 125 m, (b) the moderately nonlinear regime with drags from mountain heights of 250–1000 m, and (c) the highly nonlinear regime with mountain heights of 1250 and 1500 m.

$$\mathcal{D} = -\frac{1}{\mathcal{D}_l}\int_0^L \int_0^L P\frac{\partial h_s}{\partial x}\,dx\,dy|_{z=h_s},$$

where $\mathcal{D}_l$ is the drag for the steady-state linear solution for the same mountain with $U = 20$ m s^{-1} and $V = 0$, and $h_s(x, y)$ represents the topography. Also plotted as a function of time is $\mathcal{D}$ for the linear steady-state solution with wind speed equal to the instantaneous value of $U(t)$ at the mountain crest. Let $\varepsilon = Nh_0/U(x_0, 0, \tau/2)$ be the minimum value of the nondimensional mountain height, which during a given simulation is attained at the time of maximum wind. For mountain heights of 125 m or less ($\varepsilon < 0.0625$), the simulated pressure drag closely follows the linear steady-state solution and exhibits the same sinusoidal variation as $U(t)$ (Fig. 2a). As discussed in CDH and evident in Fig. 2b, for mountain heights in the range $250 \le h \le 1000$ m ($0.125 \le \varepsilon \le 0.5$), the drag is enhanced during the period of mean flow acceleration because the vertical group velocity of the mountain-wave packets increases as the speed of the mean flow increases. When wave packets launched later in the accelerating flow overtake those launched earlier, there is an accumulation of wave action aloft that enhances the downward momentum flux and, in the nonlinear case, also increases the cross-mountain drag. This is also evident in the time–altitude distribution of horizontally averaged momentum flux shown in Fig. 3a.

Although there is still some enhancement during the acceleration phase, the maximum drag for the highest mountains ($h \ge 1250$ m, $\varepsilon > 0.625$), occurs just after the time of maximum wind (Fig. 2c), as does the area-integrated momentum flux (Fig. 3c). The wave packet accumulation mechanism is not dominant for these higher mountains because, as shown in Fig. 3d, they are high enough to force low-level wave breaking during the entire period of significant cross-mountain flow. We expect that if a typical midlatitude westerly wind shear was added to the large-scale flow, the waves forced by the 1.5-km-high mountain would not break during the period of maximum cross-mountain flow and the wave-accumulation mechanism would again become significant. Nevertheless, throughout this paper we limit our attention to barotropic flows in order to examine the effects of wave breaking in the simplest possible context.[2]

a. Linear regime, h = 250 m (ε = 0.125)

We turn now to the budget for the absolute momentum $m = u - f\eta$, where η is the north–south displace-

[2] This is also the context (flows with constant N and U) in which wave breaking has been most extensively studied for steady mean flows.

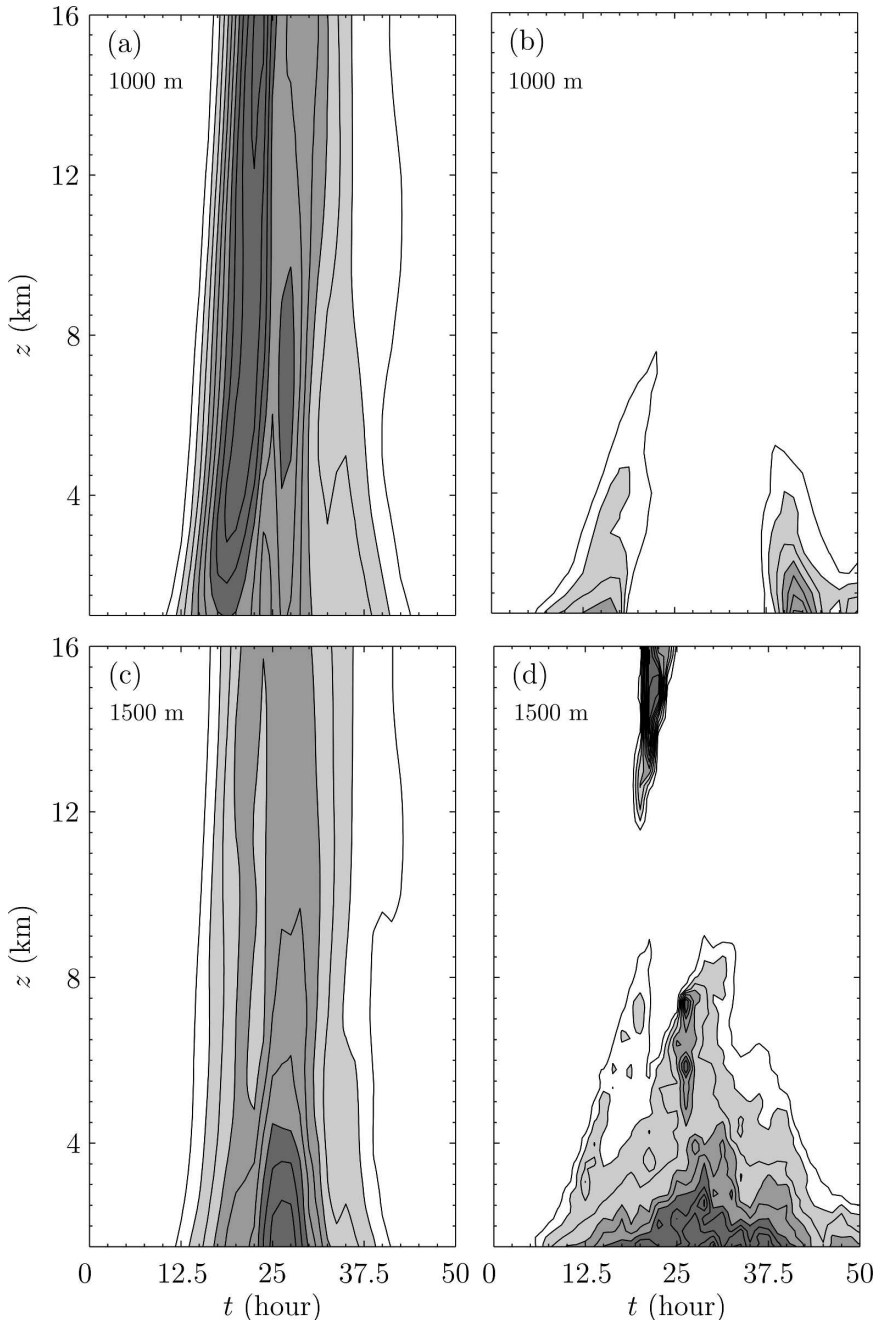

FIG. 3. Time–altitude distribution of area-integrated momentum flux $\langle \rho_0 uw \rangle$ normalized by the flux for the linear steady-state solution driven by the maximum cross-mountain flow of 20 m s^{-1}: (a) $h = 1000$ m and (c) $h = 1500$ m. Domain maximum subgrid-scale diffusivity as function of t and z: (b) $h = 1000$ m and (d) $h = 1500$ m. The three gray shades represent intensities for momentum flux at thresholds of 0.5, 1.0, and 1.75, and for subgrid-scale diffusivity at 8, 16, and 24 m^2 s^{-1}. The contour intervals for momentum flux and diffusivity are 0.25 and 4 m^2 s^{-1}, respectively.

ment of an air parcel from its initial location and a constant multiplicative factor of ρ_0 is omitted from m for notational simplicity. Using the relations $\nabla \cdot \mathbf{v} = 0$ (which is very closely approximated by the numerical solutions to our "compressible Boussinesq" system) and $D\eta/Dt = \upsilon$, the x-component of (1) may be expressed in the following form:

$$\frac{\partial m}{\partial t} + \frac{\partial m(u + u_0)}{\partial x} + \frac{\partial m\upsilon}{\partial y} + \frac{\partial mw}{\partial z} + \frac{\partial P}{\partial x} = F_x. \quad (5)$$

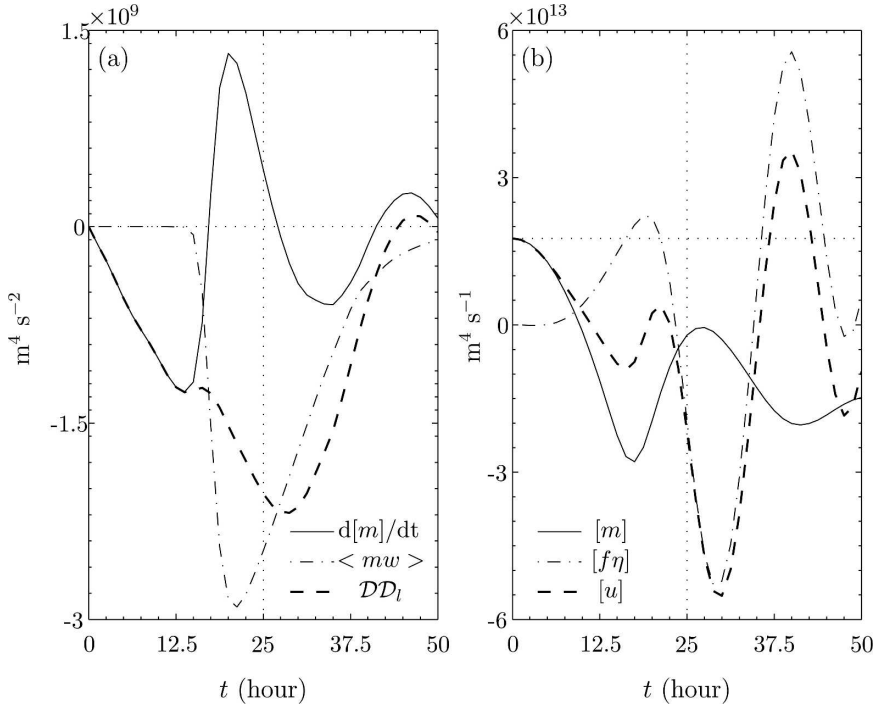

FIG. 4. Domain-integrated absolute momentum budget for the $h = 250$ m simulation as a function of time: (a) $d[m]/dt$ (solid), pressure drag (dashed), and absolute momentum flux through the top of the domain (dot–dashed) and (b) absolute momentum (solid), zonal momentum (dashed), and $f\eta$ (dot–dashed).

Let $\langle F \rangle$ denote the integral of the function F over a horizontal plane spanning the periodic computational domain,

$$\langle F \rangle = \int_0^L \int_0^L F \, dx \, dy,$$

and let $[F]$ denote the volume integral over the entire domain beneath the damping layer (which begins at $z = 16$ km):

$$[F] = \int_{h_s}^{16\text{ km}} \langle F \rangle \, dz.$$

Integrating (5) over this volume, noting that the horizontal fluxes integrate to 0 by periodicity, and neglecting subgrid-scale diffusive fluxes at the top and bottom of the volume, one obtains

$$\begin{aligned} \frac{d[m]}{dt} &= -\int_0^L \int_0^L mw \, dx \, dy|_{z=16\text{ km}} \\ &\quad - \int_0^L \int_0^L P \frac{\partial h_s}{\partial x} \, dx \, dy|_{z=h_s}, \\ &= -\langle mw \rangle|_{z=16\text{ km}} + \mathcal{D}_l\mathcal{D}. \end{aligned} \tag{6}$$

This expression implies that the rate of change of the domain-integrated absolute momentum is equal to the difference between the flux of absolute momentum through the top boundary and the pressure drag on the topography.

Each of the three terms in (6) is plotted as a function of time for the 250-m mountain simulation in Fig. 4a.[3] One might expect a symmetric response in $d[m]/dt$, with negative (positive) values during the first (second) half of the period when the pressure drag would likely be greater (less) than the momentum fluxes aloft as the cross-mountain flow increases (decreases) with time. These expectations are confirmed during the first 12 h, when the absolute momentum tendency equals the pressure drag, before significant wave activity reaches the upper boundary. The expected behavior is interrupted when the momentum flux aloft suddenly exceeds the pressure drag, and $d[m]/dt$ becomes positive around hour 17. Just 3 h later, and still several hours before the peak in surface pressure drag, the momentum fluxes at the upper boundary reach their peak. By 27 h these fluxes become weaker than the pressure drag

[3] The north–south displacement was computed by integrating the auxiliary equation $d\eta/dt = v$ during the numerical simulation.

and $d[m]/dt$ is again negative. Near the end of the simulation, weak downward momentum fluxes are still present at the upper boundary, while the pressure drag drops to 0 and even becomes negative during a brief period of reversed cross-mountain flow, so $d[m]/dt$ switches back to positive. As mentioned above, the time asymmetry in the evolution of the absolute momentum is due to wave packet accumulation during the period of mean-flow acceleration (CDH).

A similar scenario is depicted in the evolution of $[m]$, $[u]$, and $[f\eta]$ over one synoptic period (Fig. 4b). Both $[m]$ and $[u]$ are initially positive despite the square-wave structure in the initial velocity field because the volume of air displaced by the mountain, in which u is approximately -10 m s^{-1}, is not included in the domain average. There is a net decrease in $[m]$ over one period of the flow despite the virtual absence of subgrid-scale mixing in this simulation. This decrease is due to transients in our initial value problem. When the simulation is continued for another 50 h, there is still a net loss of $[m]$ over the second cycle in the large-scale flow, but the loss is only about half that generated during the first cycle.

It should be emphasized that although no permanent wave–mean flow interaction takes place in the essentially nondissipative 250-m-high mountain simulation shown in Fig. 4, temporary interactions induce relatively long-lived domain-averaged decelerations. Here we consider these long-lived impacts by extending the solutions to cover a second period of the basic state, and examining the vertical profile of time- and space-averaged vertical absolute momentum flux. For any level above the mountain, the area-integrated absolute momentum on the entire x–y plane satisfies

$$\frac{\partial\langle m\rangle}{\partial t} = -\frac{\partial}{\partial z}\langle mw\rangle,$$

and the change in the area-integrated absolute momentum after one cycle of the large-scale flow (from $t = t_0$ to $t_0 + \tau$) is determined by

$$\Delta\langle m\rangle = \langle m\rangle(t_0 + \tau) - \langle m\rangle(t_0) = -\frac{\partial}{\partial z}\int_{t_0}^{t_0+\tau}\langle mw\rangle\, dt.$$

The vertical profile of normalized absolute momentum flux $\langle mw\rangle/(\mathcal{D}'\mathcal{D}_\ell)$ averaged over the first and second 50-h periods of the synoptic-scale flow is plotted in Fig. 5. Consistent with a gradual approach to a purely periodic solution, the vertical gradient in the flux is weaker during the second period of the flow. Nevertheless, the vertical divergence associated with these absolute momentum flux profiles implies that, even without wave breaking, the time- and space-averaged cross-mountain flow will decelerate over both periods (more than 4 days). Ultimately those gravity waves not associated with a strictly time-periodic solution should propagate vertically through the upper boundary of the domain, and the net change in $[m]$ over each synoptic-scale period should drop to 0.

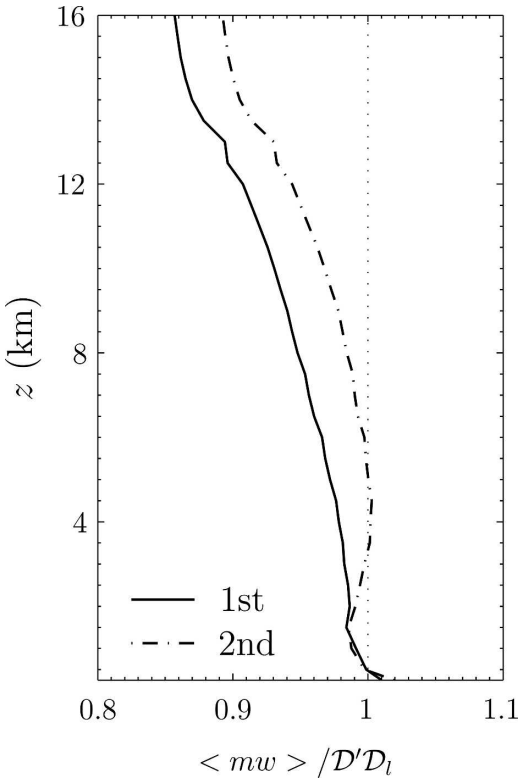

FIG. 5. Vertical profile of $\langle mw\rangle$ averaged over one period of the synoptic-scale flow and normalized by the mesoscale cross-mountain pressure drag averaged over the same period for h = 250 m. The solid line shows the average over the first period and the dot–dashed line shows the average over the second period.

Further details about the time variations in the mean zonal and meridional flows may be diagnosed by averaging of the horizontal momentum equations in x and y, recalling that the horizontal domain is periodic and neglecting subgrid-scale diffusive fluxes:[4]

$$\frac{\partial\langle u\rangle}{\partial t} - f\langle v\rangle = -\frac{\partial}{\partial z}\langle uw\rangle, \tag{7}$$

$$\frac{\partial\langle v\rangle}{\partial t} + f\langle u\rangle = -\frac{\partial}{\partial z}\langle vw\rangle. \tag{8}$$

Combining (7) and (8) yields an equation governing the behavior of the zonal-mean flow:

[4] Even in the presence of wave breaking, the diffusive fluxes do not play a major role in the global momentum budgets.

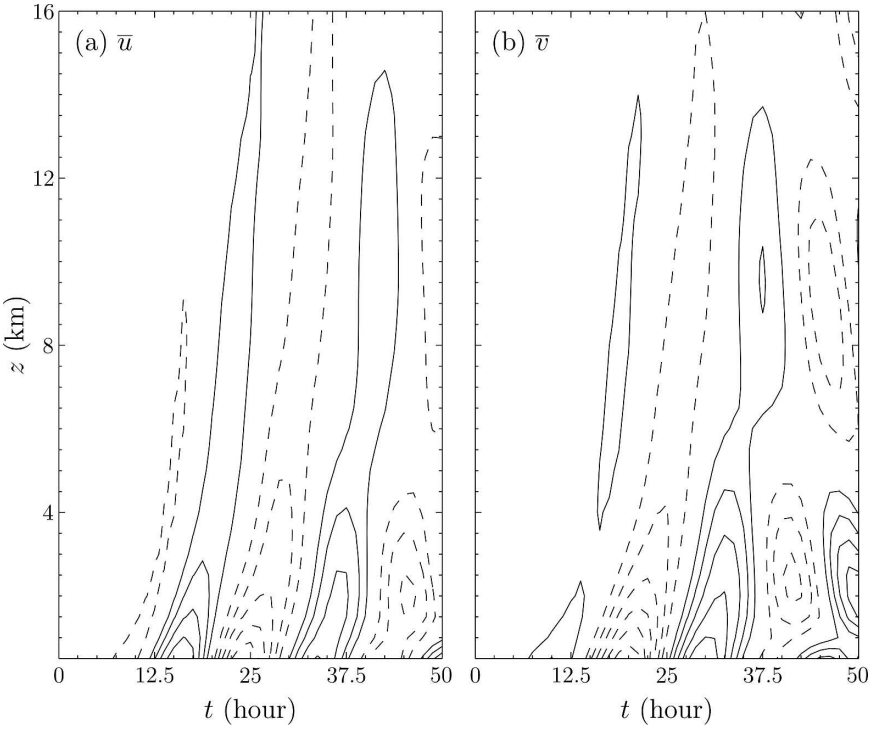

FIG. 6. Time–altitude distribution for $h = 250$ m of the (a) mean zonal velocity $\langle u \rangle$, and (b) meridional velocity $\langle v \rangle$ at contour intervals of 7.5×10^{-4} m s^{-1}; dashed contours denote negative values.

$$\frac{\partial^2 \langle u \rangle}{\partial t^2} + f^2 \langle u \rangle = -\frac{\partial}{\partial t}\frac{\partial}{\partial z}\langle uw \rangle - f\frac{\partial}{\partial z}\langle vw \rangle. \qquad (9)$$

Homogeneous solutions of (9) take the form of $\cos(ft)$ and $\sin(ft)$, suggesting that the evolution of $\langle u \rangle$ may project onto inertial oscillations (Lott 2003). Evidence of such a response is given in Fig. 6, which shows that the distributions of the zonal and meridional mean flow oscillate with a period of roughly 17.5 h, corresponding to the inertial period ($\sim 2\pi/f$). The origin of this oscillation appears to relate to the increase of westerly momentum around hour 15 due to the wave-accumulation process; the meridional wind then decelerates in response.

b. Nonlinear regime, $h = 1.5$ km ($\varepsilon = 0.75$)

Since the dynamics of the synoptic-scale flow prescribed in this study are well understood in the absence of a mountain, the spatial flow response induced by the mesoscale mountain may be examined by defining difference fields (i.e., departures from the flow fields from the control solution in the absence of the mountain). Velocity and PV difference fields are defined as

$$u' = u + u_0 - U, \quad v' = v - V, \quad w' = w,$$

$$q' = q - Q = (\nabla \times \mathbf{v} + f\hat{\mathbf{k}}) \cdot \nabla\theta - Q,$$

where Q is the Ertel PV of the large-scale flow:

$$Q = \left(\frac{\partial V}{\partial x} - \frac{\partial U}{\partial y} + f\right)\frac{\partial \theta_r}{\partial z}.$$

As will be discussed in section 7, q' may be produced through purely adiabatic and nondissipative processes due to internal dynamics (e.g., gravity waves), but here we focus on the strong signal in q' arising from nonadiabatic processes in breaking gravity waves over a 1.5-km-high mountain.

Comparing the zonally averaged q' and u' fields plotted in Fig. 7 shows a compact region with reduced zonal momentum near the mountain surrounded by broader and weaker regions of acceleration. This pattern is in good qualitative agreement with the zonally averaged PV field that features negative (positive) PV on the north (south) side of the mountain; we defer a quantitative analysis of this relationship until later in the paper.

4. Three-dimensional structure of the mountain-induced perturbations

To expose the processes and locations responsible for the large-scale changes apparent in the previous section, relevant aspects of the full three-dimensional

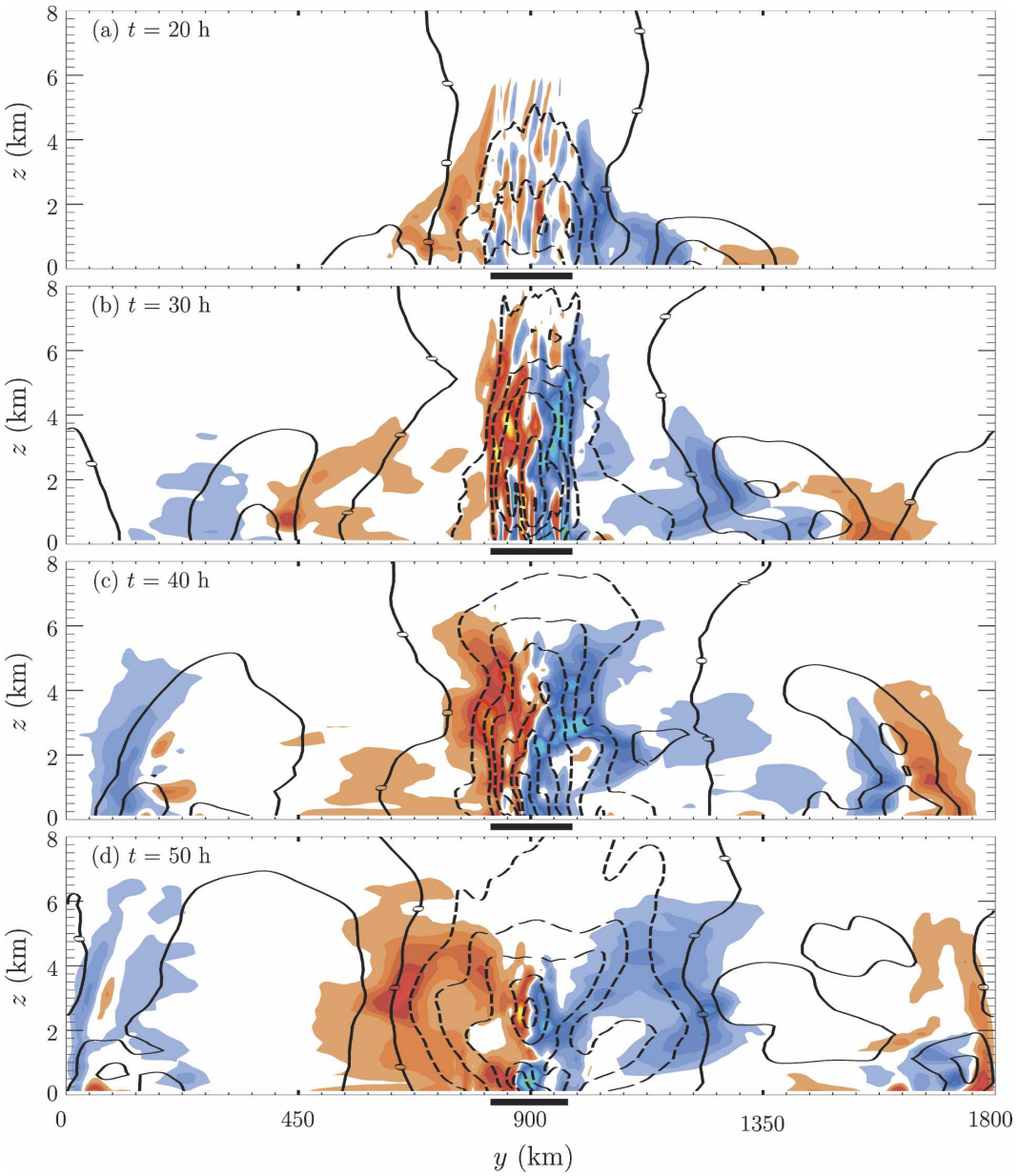

FIG. 7. The zonal average of q' (color shading) and u' (black lines) as a function of y and z for $h = 1.5$ km at times: (a) 20, (b) 30, (c) 40, and (d) 50 h. The contour intervals for q' and u' are 10^8 K m^{-1} s^{-1} and 0.5 m s^{-1}, respectively. Red (blue) shades denote positive (negative) PV and solid (dashed) lines represent flow acceleration (deceleration). The location of the mountain range is indicated by a thick line beneath the x axis. The contribution from the background PV has been removed from the zonal-averaged PV.

structure of the solutions are now explored. In the following, we focus on the 1.5-km mountain because, except for the first few hours when the flow is blocked, turbulent mixing persists in the low- to midtroposphere throughout the simulation, causing PV production as well as intense wave–mean flow interaction.

Several previous studies (Schär 1993; Schär and Durran 1997; Rotunno et a1. 1999) have demonstrated that PV anomalies may be produced in the lee of a mountain in the presence of wave dissipation. The PV evolution is governed by

$$\frac{Dq}{Dt} = (\nabla \times \mathbf{v} + f\hat{\mathbf{k}}) \cdot \nabla H + [\nabla \times \mathbf{F}] \cdot \nabla \theta, \qquad (10)$$

which indicates that the turbulent subgrid-scale fluxes of momentum $\mathbf{F}$ and heat H are responsible for PV

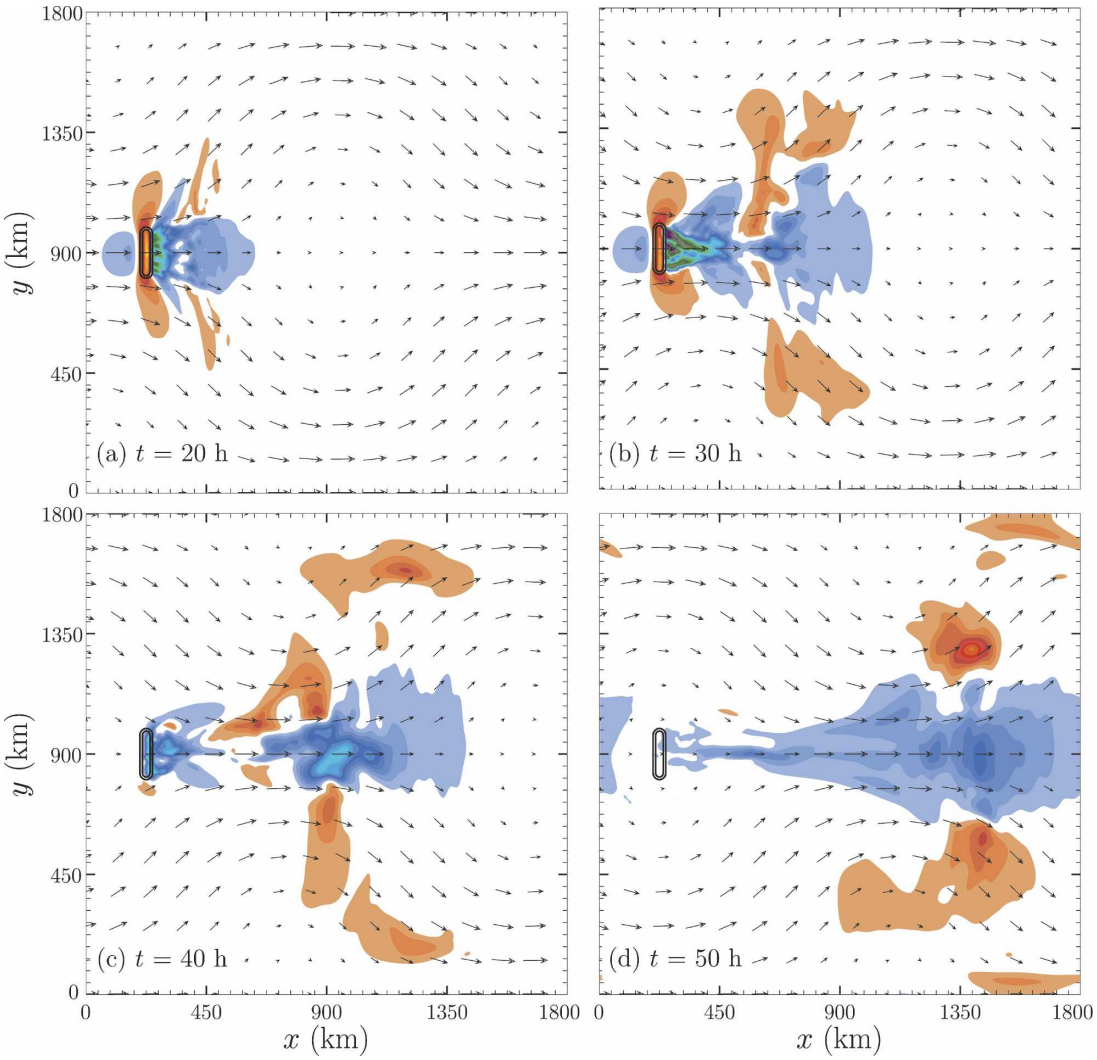

FIG. 8. The u' field forced by a 1.5-km mountain, in color shading with a contour interval of 1 m s^{-1}, on an x–y plane at z = 3 km at times: (a) 20, (b) 30, (c) 40, and (d) 50 h. Blue (red) shades denote flow deceleration (acceleration). The background velocity field (U, V) is denoted by black arrows.

generation. However, the model also uses a numerical filter that suppresses grid-scale noise to prevent nonlinear numerical stability. For the highly nonlinear case considered here, a horizontal resolution of 6 km is not adequate since the PV production associated with the numerical filter is comparable to that associated with terms representing the physical generation of PV through subgrid-scale mixing. We therefore employ a two-level interactive grid nest in which a fine grid is placed over the mountain with a horizontal resolution of 2 km, so that nonphysical PV production is reduced to less than 10% of the physically based production. The fine mesh, whose extent is shown in Fig. la, occupies the region $105 \le x \le 545$ km and $540 \le y \le 1260$ km.

The spatial distribution of u' at z = 3 km is plotted in Fig. 8, for the same times as in Fig. 7. Near the mountain the u' field is dominated by a strong gravity wave signal. There are, however, larger-scale perturbations that move coherently far downstream of the mountain. At the end of the cycle, t = 50 h, a broad region with flow deceleration is centered at (x, y) = (1400, 900) km (Fig. 8d) and the strongest flow deceleration exceeds -5 m s^{-1}. The region of strong flow deceleration is almost collocated with the 20 m s^{-1} jet in the large-scale flow, implying that after one complete cycle this jet is significantly slowed down due to the presence of the mountain. Conversely, patches of flow acceleration are also found, mostly north and south of the main region of flow deceleration. This is consistent with the zonal-average field shown in Fig. 7.

Throughout the simulation, PV is generated by persistent turbulent mixing in the lee of the mountain (see

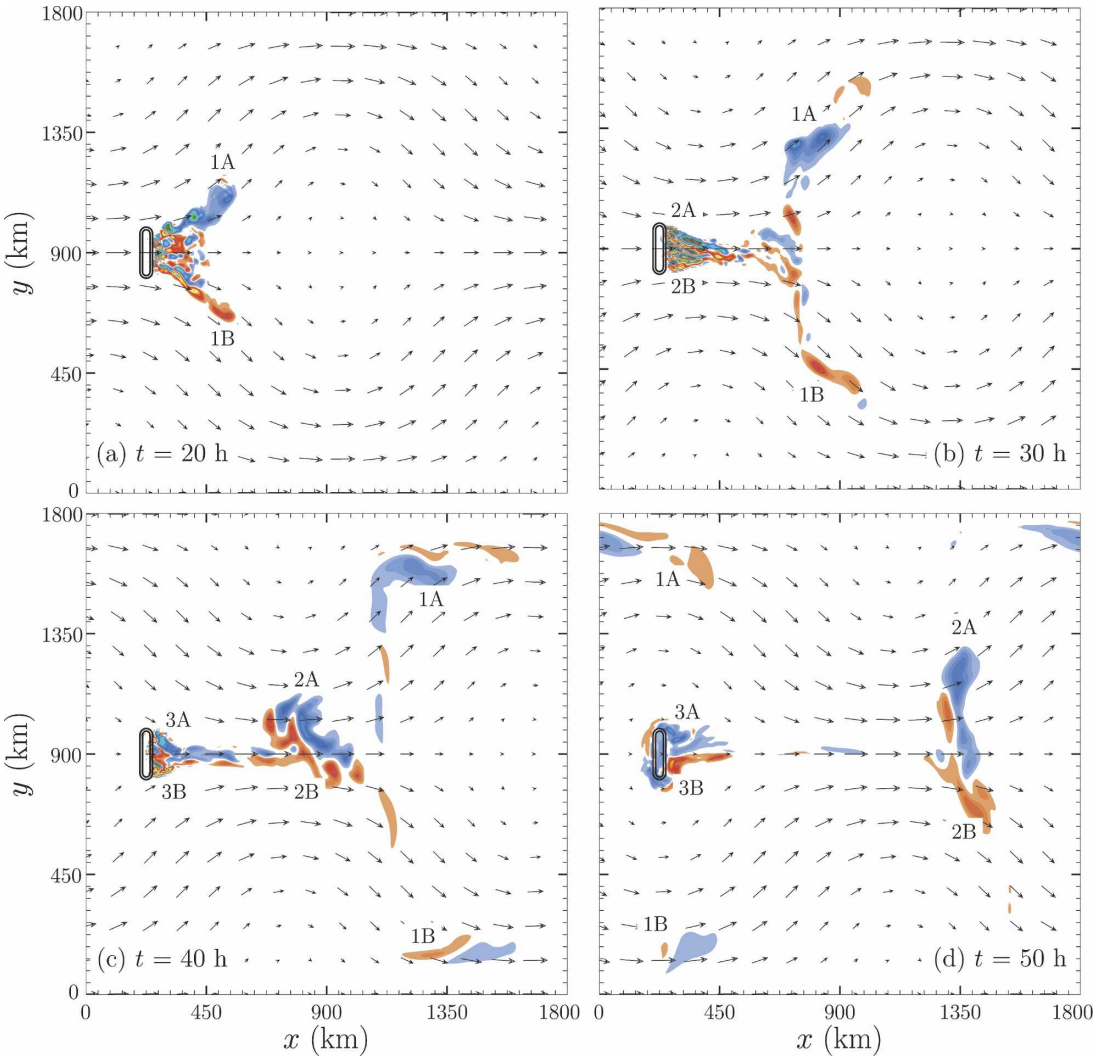

FIG. 9. The Ertel PV difference field forced by a 1.5-km mountain, in color shading with a contour interval of 10^{-7} K m^{-1} s^{-1}, on an x–y plane at z = 1.5 km at times: (a) 20, (b) 30, (c) 40, and (d) 50 h. Blue (red) shadings denote negative (positive) PV. The background velocity field (U, V) is denoted by black arrows. Here (1A–1B), (2A–2B), and (3A–3B) denote three major groups of PV anomalies generated during the simulation.

Fig. 3d). Unlike the simple PV dipole found behind circular mountains in earlier studies by Schär and Durran (1997) and Rotunno et al. (1999), the wake for this elongated ridge is flanked by extrema of opposite sign in the PV field surrounding a more complex distribution of smaller-scale PV anomalies within the interior of the wake (Fig. 9). Away from the mountain, the flow is nearly inviscid and adiabatic, and the PV anomalies are passively advected by the synoptic-scale flow field.[5]

Three pairs of organized PV anomalies appear in the wake of the mountain; they are labeled as (1A–1B), (2A–2B), and (3A–3B) in Fig. 9. Pair (1A–1B) first appears around hour 20 during the accelerating phase of the synoptic-scale flow. These anomalies are subsequently separated meridionally by the difluent flow as they move downstream of the mountain. Pair (2A–2B) appears around hour 30, which is a time of deep turbulent mixing (Figs. 3d and 12c). This PV dipole possesses a deeper structure than the first pair (not shown) and, as will be shown in section 5, pair (2A–2B) turns out to be responsible for the major flow deceleration located far downstream of the mountain at the end of the cycle. Pair (3A–3B) appears around hour 40, during a time of

[5] The subsequent locations of PV anomalies initially generated near the mountain are well predicted by trajectory calculations derived from the background large-scale velocity field (U, V).

flow deceleration and confluence in the synoptic-scale wind field. Unlike the previous two PV pairs, the ambient wind is too weak to allow (3A–3B) to separate from the mountain, and their movement is dominated by their mutual interaction, which forces them to move westward toward the mountain. In fact, the reverse flow associated with (3A–3B) eventually overwhelms the background flow, turning the eastern slope of the mountain into the windward side, and the pressure drag switches signs at 47.5 h (Fig. 2c). A similar reversal in the pressure drag is also found near $t = 50$ h for the 1- and 1.25-km-high mountains (Figs. 2b,c).

5. Potential vorticity inversion

As suggested by Fig. 7, the spatial distribution of the perturbation zonal momentum field seems to be in good agreement with what is implied by the perturbation PV field. This motivates us to quantify the agreement through PV inversion. The full difference velocity field is divided into balanced and unbalanced portions. The balanced part, $\mathbf{u}_b' = (u_b', v_b')$, is defined here through PV inversion using geostrophic balance as the balance constraint. We apply doubly periodic lateral boundary conditions in the horizontal, and homogeneous (inhomogeneous) Neumann conditions at the top (bottom) boundaries; the lower boundary condition is derived from the perturbation surface potential temperature.

Rather than invert the quasigeostrophic potential vorticity, we opt instead for inverting a scaled version of the Ertel PV, which allows for error in recovering the mass field. In this case, the streamfunction ψ satisfies

$$\frac{q'}{\partial\theta_r/\partial z} = \frac{\partial^2\psi}{\partial x^2} + \frac{\partial^2\psi}{\partial y^2} + \frac{f^2}{N^2}\frac{\partial^2\psi}{\partial z^2}, \tag{11}$$

and

$$u_b' = -\frac{\partial\psi}{\partial y}, \quad v_b' = \frac{\partial\psi}{\partial x}. \tag{12}$$

Successive overrelaxation (SOR) is used to solve (11) for ψ; terminating when successive iterations generate no changes in the velocity field larger than 10^{-5} m s^{-1}.

The inverted zonal velocity field at $z = 3$ km is presented in Fig. 10 for the same times shown in Figs. 7–9. The u_b' field is in good agreement with the full u' field (cf. Fig. 8), especially far from the mountain. The good agreement between u_b' and u' implies that a large portion of the difference fields can be understood by PV dynamics, although as expected, u_b' fails to capture the strong gravity waves generated in the immediate vicinity of the mountain.

At 20 h, the good agreement between Figs. 8a and 10a confirms that the region of flow deceleration centered at (450, 900) km is in balance with the PV anomalies created early in the cycle, denoted as (1A–1B) in Fig. 9a. At 30 h, (1A–1B) continue to be associated with the leading edge of the spatial response in the perturbation velocity, which has progressed to $x \sim 900$ km (Figs. 8b, 9b, and 10b). Closer to the mountain, the balanced response (u_b') is characterized by intense flow deceleration along the centerline (Fig. 10b), with patches of flow acceleration immediately downstream of the flanks of the mountain. These regions of intense u_b' are associated with PV anomalies (2A–2B) evident in Fig. 9b. PV anomalies (2A–2B) continue to produce significant flow deceleration/acceleration centered at (900, 900) km at 40 h (Figs. 8c, 10c) and at (1400, 900) km at 50 h (Figs. 8d, 10d). At these later times, the influence of (1A–1B) is limited to the northern and southern edges of the domain and is characterized by two patches of strong flow acceleration. It is interesting to note that no strong flow deceleration is present at 50 h close to the mountain (see Figs. 8d and 10d) as might be expected to occur in association with with PV dipole (3A–3B) shown in Fig. 9d. This is because the vertical structure of (3A–3B) is too shallow to create anomalies that penetrate up to $z = 3$ km. The influence of (3A–3B) is therefore limited to lower levels.

At 50 h the balanced response is mostly due to PV anomalies (2A–2B), which were generated shortly after the time of strongest cross-mountain flow (hours 25–30). Initially, the strongest PV perturbations associated with (2A–2B) are found between $z = 1.5$ and 6 km (see Fig. 7b) and the vertical average of the perturbation PV field between these two levels is plotted at $t = 50$ h in Fig. 11a. Due to this vertical averaging, both (1A–1B) and (3A–3B) almost vanish since these anomalies are shallow and mainly confined below the mountain height (1.5 km). To separate the influence of (2A–2B) from other PV anomalies, we employ piecewise PV inversion, considering only those PV perturbations residing in the layer between $z = 1.5$ and 6 km and within the box outlined by the thick black line in Fig. 11a; all other PV anomalies are discarded and homogeneous boundary conditions are employed. The result (Fig. 11b) is in excellent agreement with the full difference field (Fig. 8d) in the region of flow deceleration and acceleration centered at (1400, 900) km, confirming that the intense PV anomalies created near the mountain between 25 and 30 h play a key role in producing the main large-scale velocity perturbations at the end of the cycle. There are, nevertheless, some differences in u_b' recovered by the full PV inversion and by piecewise PV inversion. For example, the two patches of flow

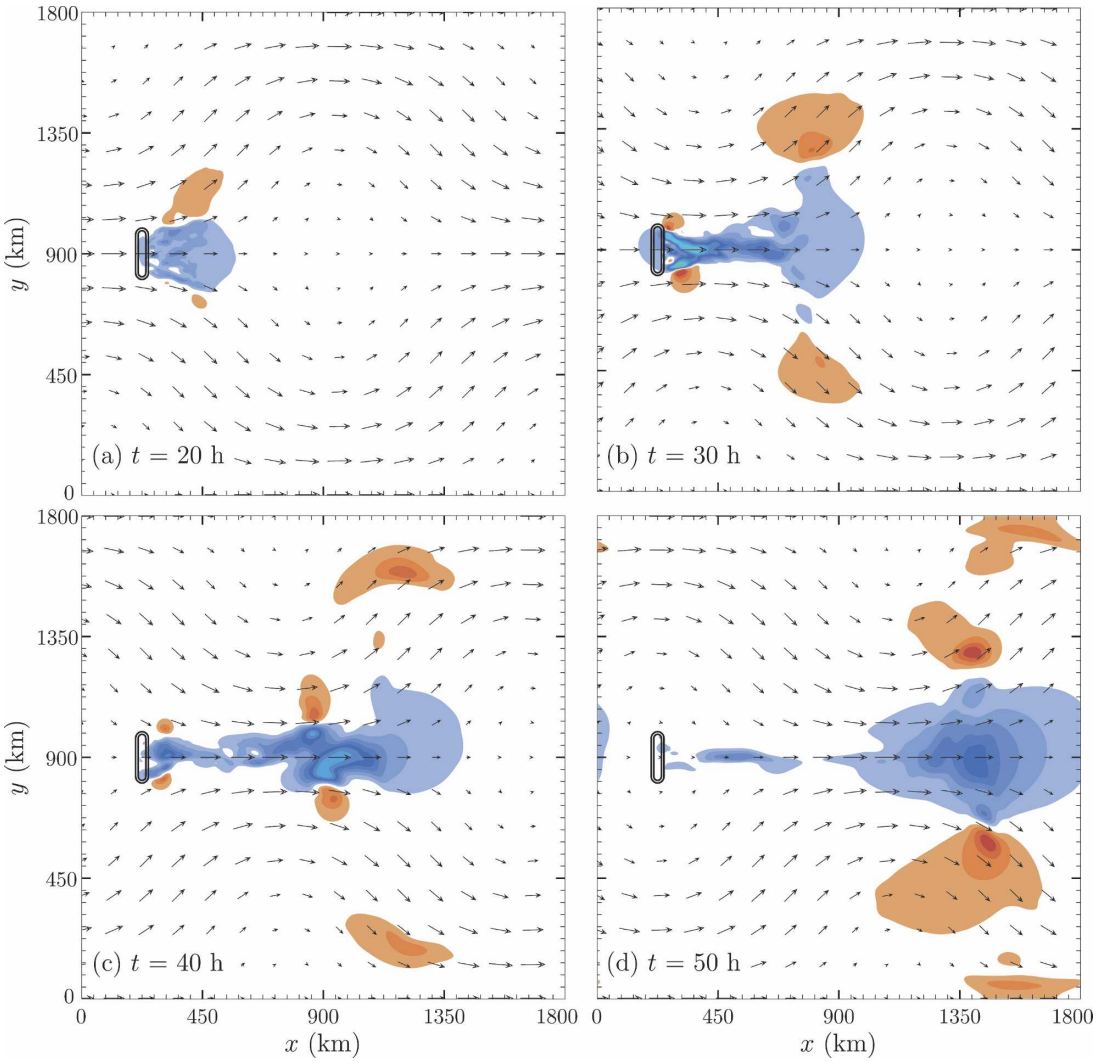

FIG. 10. Same as in Fig. 8, but the contoured field is the balanced zonal velocity u_b', obtained by inverting the full Ertel PV difference field.

acceleration located at the northern and southern boundaries found in Fig. 10d but not in Fig. 11b are associated with the PV anomalies generated at the early stage of the cycle (1A–1B). There also exists a region with flow deceleration downstream of the mountain, centered at (500, 900) km (Fig. 10d), which is missing in the flow field recovered by piecewise PV inversion because it is associated with PV anomalies generated much later in the cycle that remain well upstream of the boxed region in Fig. 11a.

These results show that extensive regions of significant geostrophically balanced large-scale perturbations in the zonal momentum field can be generated by breaking mountain waves. Yet as evident from (12), since our domain is periodic, *the horizontal integral of these perturbations is 0.* As will be discussed in section 8, most gravity wave–drag parameterizations focus on capturing the influence of the mountain on area-averaged u' and may therefore dramatically underestimate the strength and structure of the synoptic-scale geostrophically balanced response.

6. Potential vorticity sources

As demonstrated in the previous section, PV anomalies originating between 25 and 30 h, labeled as (2A–2B) in Fig. 9, exert an important influence on the large-scale flow. Here we explore the source of these PV anomalies. During the period of accelerating cross-mountain flow, a region with turbulent mixing develops near the ground, but remains relatively shallow (Figs. 12a,b). As the large-scale cross-mountain flow begins to

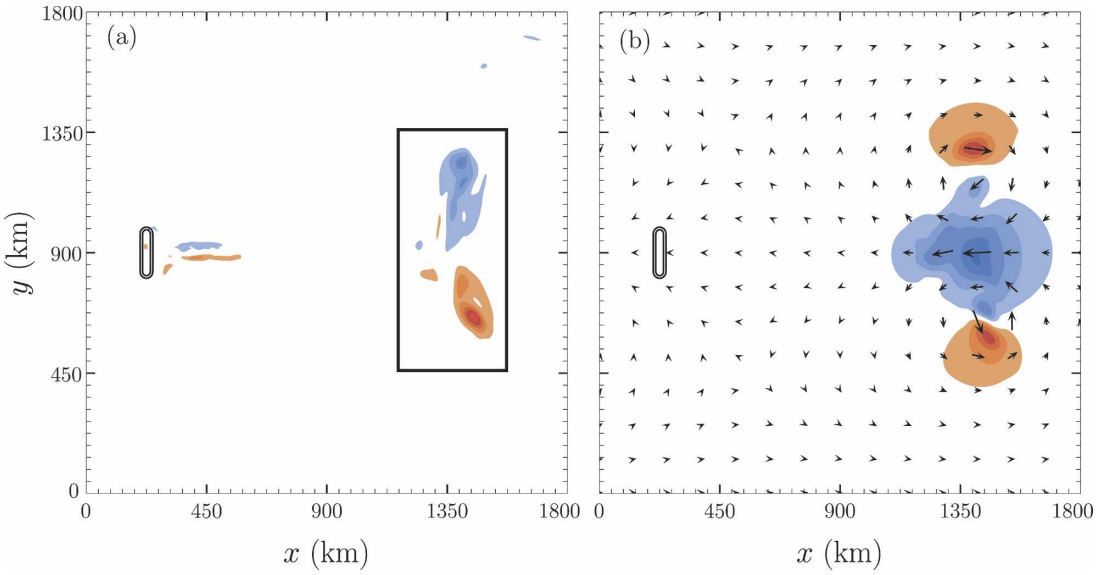

FIG. 11. (a) The perturbation Ertel PV field forced by a 1.5-km mountain at $t = 50$ h, averaged between $z = 1.5$ and 6 km with a contour interval of 10^{-7} K m^{-1} s^{-1}; (b) u_b', denoted by color shading with a contour interval of 1 m s^{-1}, and $\mathbf{u}_b'$, denoted by black arrows (maximum vector length is 5 m s^{-1}), recovered by piecewise PV inversion by using the perturbation PV field from $z = 1.5$–6 km residing in the region in (a) denoted by a thick black line. Blue (red) shadings denote negative (positive) values.

decelerate, the waves launched by the mountain at earlier times begin to propagate upstream, leading to enhanced horizontal temperature gradients in the main mountain-wave trough and wave breaking in a region of weaker static stability farther downstream. As is evident in Fig. 12c, at 30 h a deep layer of turbulent mixing is present between the ground and about 5 km. This region of turbulent mixing is deepest between hours 25 and 30 (Fig. 3d), precisely the time during which the deepest PV anomalies (2A–2B) develop. Shortly thereafter the wave-breaking region collapses into a shallower layer (Fig. 12d).

The aggregate effect of turbulent mixing in the lee of the mountain may be related to the generation of PV by examining the distribution of the perturbation Bernoulli function B on isentropic surfaces. The local rate of change of Ertel PV is given by the divergence of the vector field $\mathbf{J}$ (Schär 1993):

$$\frac{\partial q}{\partial t} + \nabla \cdot \mathbf{J} = 0,$$

where

$$\mathbf{J} = \nabla\theta \times \nabla B, \tag{13}$$

and in our Boussinesq system:

$$B = \frac{1}{2}(\mathbf{v} + u_0\mathbf{i}) \cdot (\mathbf{v} + u_0\mathbf{i}) + P + P_g - g\frac{\theta - \theta_r}{\theta_0} - \frac{1}{2}N^2z^2.$$

For steady flows, (13) implies that $\mathbf{J}$ is parallel to the intersection of surfaces of constant B and θ. Although our solutions are not completely steady, the evolution of the large-scale flow is slow enough to allow the qualitative application of (13). Figure 13a shows the distribution of B averaged over the isentropic surfaces between 292 and 298 K (roughly between the elevations of 1.5 and 3.5 km) at hour 30. A pronounced deficit in the Bernoulli function appears in a roughly triangular region in the lee of the mountain.

The gradients of B on this averaged isentropic surface are proportional to the PV flux, which in general is the sum of both advective and nonadvective fluxes. As discussed in Schär and Durran (1997) the decrease in B at the upstream edge of the wave-breaking region is associated with a nonadvective flux of PV directed southward, roughly parallel to the ridgeline. The gradients of B within the central portion of the wake are associated with a mix of advective and nonadvective PV fluxes that tend to homogenize the patches of PV generated by intense, but intermittent episodes of wave breaking over the lee slope. Downstream of the mountain, along the outside edges of the wake, the turbulence abates and the gradients in B are associated with purely advective PV fluxes. The positive (negative) fluxes at the southern (northern) edges of the wake are associated with positive (negative) PV perturbations embedded in the strong downstream flow along the edges of the wake (Fig. 13b). Between hours 25 and 30,

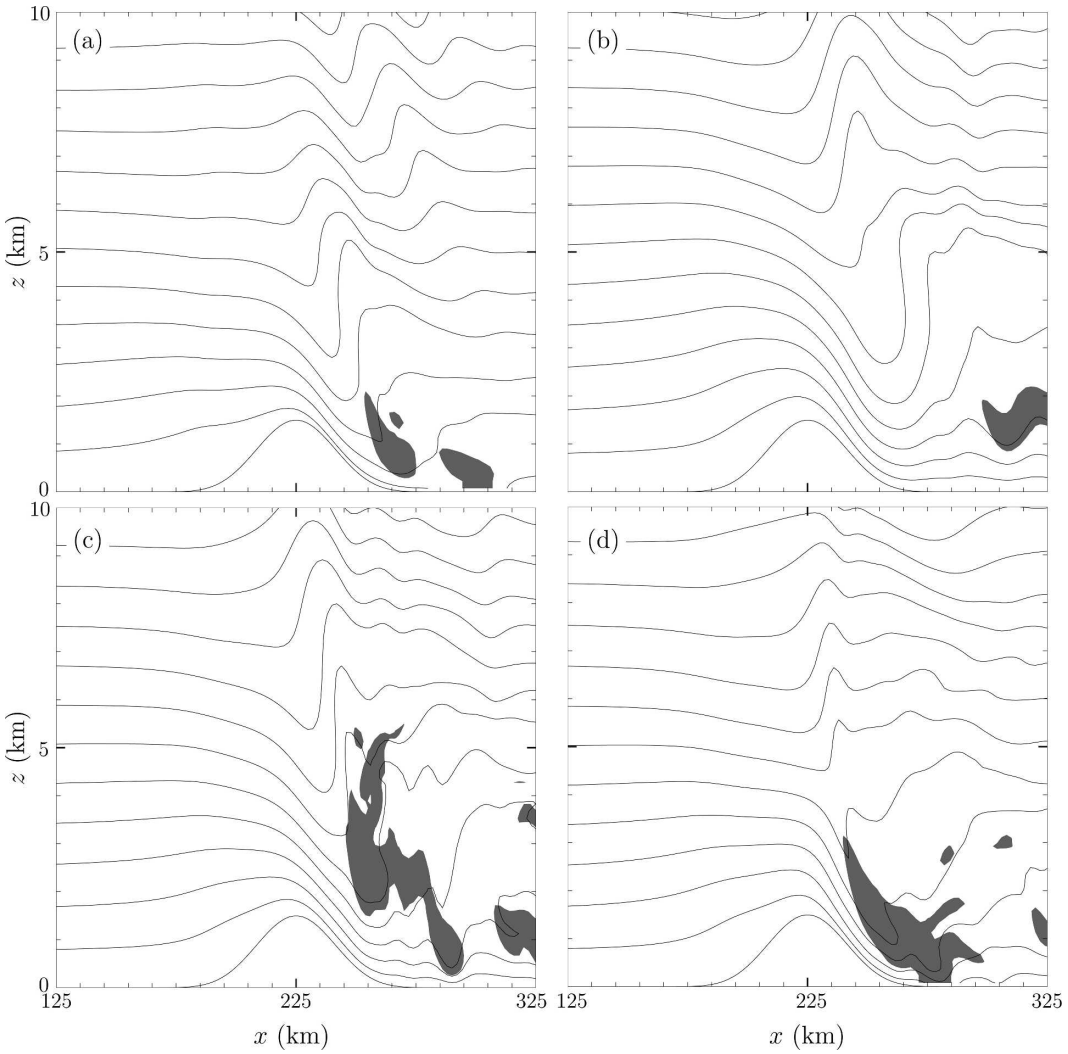

FIG. 12. Four x–z cross sections along the centerline of the mountain showing the potential temperature in thin lines for $h = 1.5$ km at $t =$ (a) 15, (b) 23.75, (c) 30, and (d) 33.75 h, respectively. The contour interval is 2.5 K and regions with subgrid-scale diffusivities exceeding 12 $m^2 s^{-1}$ are denoted by gray shading.

wave breaking continually supplies PV to the upstream edge of each of these PV perturbations. After the depth and intensity of the wave breaking is reduced, these PV perturbations are carried downstream as the anomalies (2A–2B).

7. Zonally averaged momentum

We return now to a zonally averaged perspective and explore the perturbation momentum fields u' and u'_b as a function of mountain height. Figure 14 shows y–z plots of the zonal average of u' generated by ridges ranging in height from $h = 125$ m to 1.5 km. In order that the results shown in all panels are of similar magnitude assuming a nearly linear response in mountain height, the contour interval in these plots scales with h with one exception: for legibility, it was necessary to increase the contour interval in the 1.5-km mountain case by a factor of 1.5 relative to the linear scaling. Three distinct patterns are visible in the zonally averaged u' field. One is a residual gravity wave signature emanating from the edges of the ridge (and also from perturbations created early in the simulation that have been transported near the northern and southern boundaries of the domain). The gravity wave signal scales almost linearly with mountain height for $h \leq 500$ m, and is still apparent in the $h = 1$ km case. Since gravity waves carry zero linear PV, the residual gravity wave signature is absent in the zonally averaged u'_b field (Fig. 15).

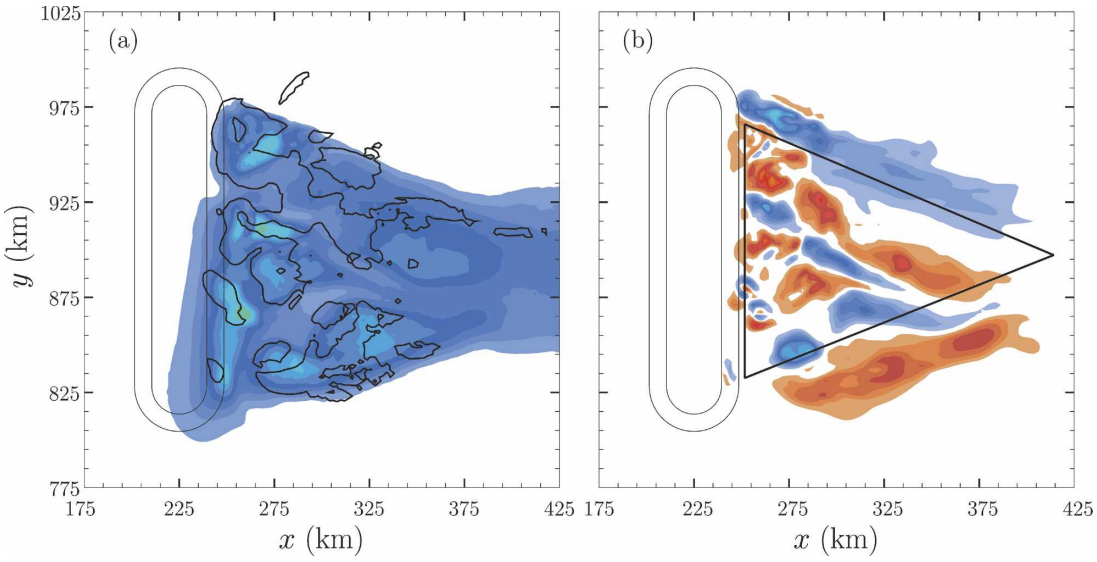

FIG. 13. (a) The average perturbation isentropic Bernoulli function B at $t = 30$ h between $\theta = 292$ and 298 K in color shading for $B < 50$ m^2 s^{-2} with a contour interval of 25 m^2 s^{-2}, and regions with average subgrid-scale diffusivity greater than 12.5 m^2 s^{-2} are denoted by thick black lines. (b) The 292–298-K average perturbation Ertel PV at $t = 30$ h with a contour interval of 5×10^{-7} K m^{-1} s^{-1}. The mesoscale mountain is denoted by thin black lines. Blue (red) shadings denote negative (positive) values. The bold black line in (b) represents a subjectively selected region with a large Bernoulli function deficit. The thin black lines are topographic contours at elevations of 500 and 1000 m.

The other two signatures in the zonal averages of u' are very similar to those in u'_b, indicating that both are balanced responses to the mountain-induced circulations. One pattern is symmetric in y and the other antisymmetric. The symmetric pattern, which is most evident when the mountain is high ($h = 1$ or 1.5 km), exhibits strong deceleration throughout the middle third of the domain, with weaker acceleration to the north and south. The symmetric signal is the balanced response to wave dissipation and the generation of a PV dipole in the lee of the mountain (cf. Fig. 7d). Wave breaking is clearly a nonlinear process and this nonlinearity is responsible for the faster-than-linear intensification of the symmetric zonal momentum perturbations between the $h = 1$ and 1.5 km cases. The maximum zonally averaged mean-flow deceleration is about 2 m s^{-1} (relative to the unperturbed mean of 10 m s^{-1}) in the $h = 1.5$ km case.

In contrast, the antisymmetric signature in the zonally averaged u' and u'_b is most apparent when the mountains are too small to generate much wave breaking ($h \leq 500$ m). In the antisymmetric case there is acceleration south of the mountain and deceleration to the north. Since there is essentially no dissipation for $h = 125$ m, a different mechanism is required to account for the asymmetric response. It appears that this pattern is generated by a PV anomaly associated with warm surface temperatures that form to the lee of the mountain early in the simulation when air parcels initially over the mountain having high potential temperature are advected downstream by the accelerating flow. This warm anomaly moves off the mountain following the leading edge of the large-scale jet, and induces a cyclonic circulation that tends to move the downstream (upstream) large-scale PV pattern northward (southward). The resulting transport tends to produce positive zonally averaged q' near the north–south center of the domain, and the acceleration–deceleration patterns induced by such an anomaly are qualitatively in accord with those observed.

Note that although the balanced response over the mountain quickly becomes anticyclonic, the circulation induced by the mountain anticyclone remains fixed relative to the evolving flow. Therefore, the sign of the PV advection induced by the mountain anticyclone oscillates on the same time scale as the large-scale flow, and little net PV transport is produced by this feature over the full 50-h cycle.

8. A "perfect" GWD parameterization experiment

Here we explore how well the spatial flow response presented earlier may be reproduced by a simple, yet in many respects "perfect," GWD parameterization scheme. Most current GWD parameterizations attempt to estimate the vertical profile of the horizontally averaged momentum fluxes $\langle \rho_0 u'w' \rangle$ and $\langle \rho_0 v'w' \rangle$, and then include the vertical divergence of these fluxes as

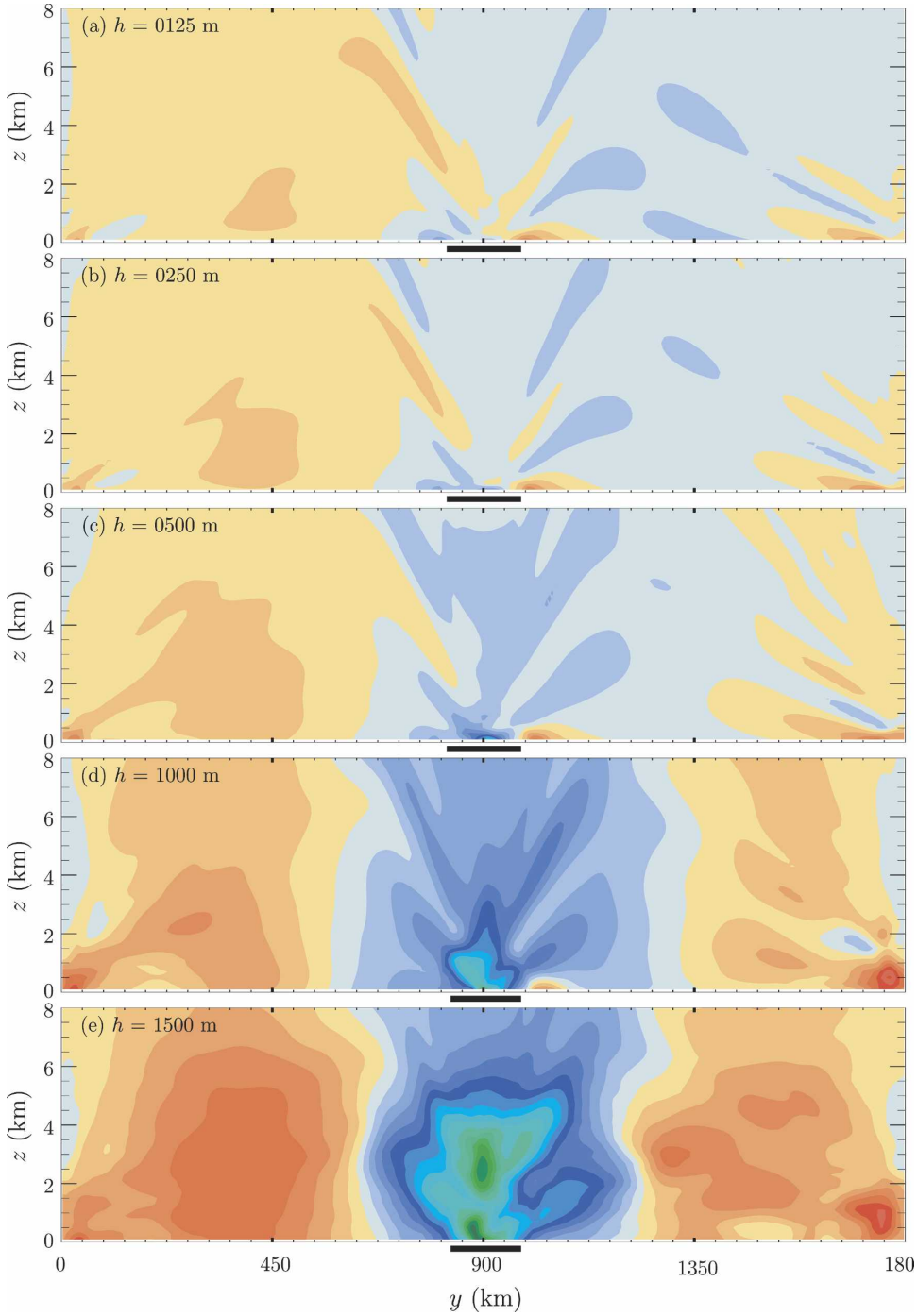

FIG. 14. The zonal average of u' at 50 h as a function of y and z for h = (a) 125, (b) 250, (c) 500, (d) 1000, and (e) 1500 m. The contour intervals for the five panels are 0.01, 0.02, 0.04, 0.08, and 0.18 m s^{-1}, respectively. The thick black line along the x axis denotes the position of the mountain range.

forcings in the u and v momentum equations, respectively. The exact values of $\langle \rho_0 u'w' \rangle$ and $\langle \rho_0 v'w' \rangle$ are available during our simulations, so it is possible to store these fluxes and then to impose them in a second simulation without a mountain. This amounts to a perfect GWD parameterization in the sense that we do not need to make any approximations to arrive at the correct momentum flux profiles, and as a consequence, the z–t dependence of $\langle u \rangle$ and $\langle v \rangle$ in the no-mountain case will closely match that in the original simulation.

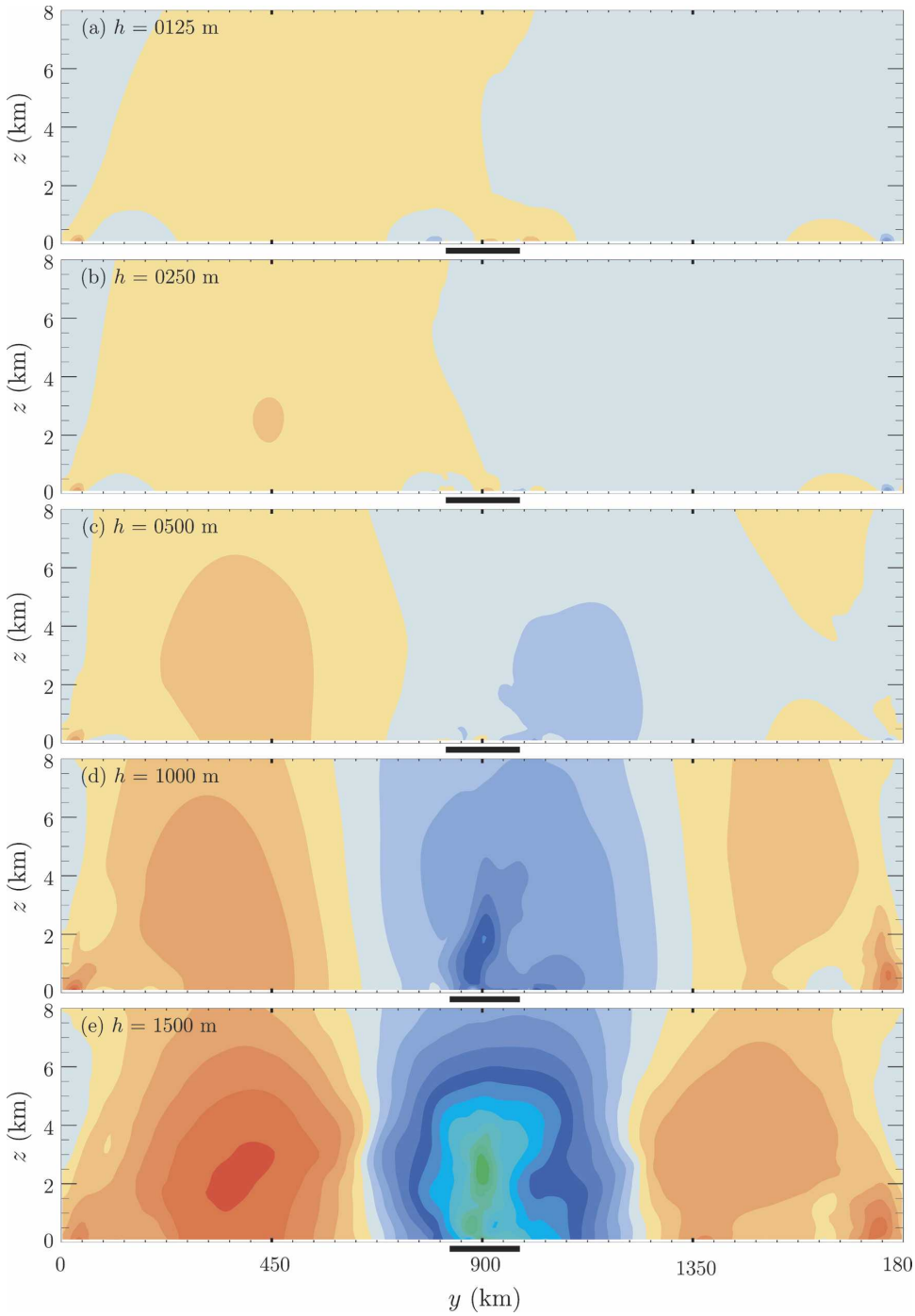

FIG. 15. Same as in Fig. 14, but for the balanced perturbation zonal velocity u'_b.

The momentum flux profiles for the $h = 1.5$ km case were saved and then imposed in a second no-mountain simulation with a coarser horizontal resolution of 18 km. As such, this represents a test of gravity wave drag parameterizations on a scale similar to that currently being approached by very high-resolution global atmospheric models. Assuming the mountains are located in a compact region whose area is A, the (Boussinesq) GWD forcing (F_x, F_y) exerted on each grid cell within the mountainous area is specified as

$$F_x(z, t) = -\frac{1}{A}\frac{\partial\langle u'w'\rangle}{\partial z}, \quad F_y(z, t) = -\frac{1}{A}\frac{\partial\langle v'w'\rangle}{\partial z},$$

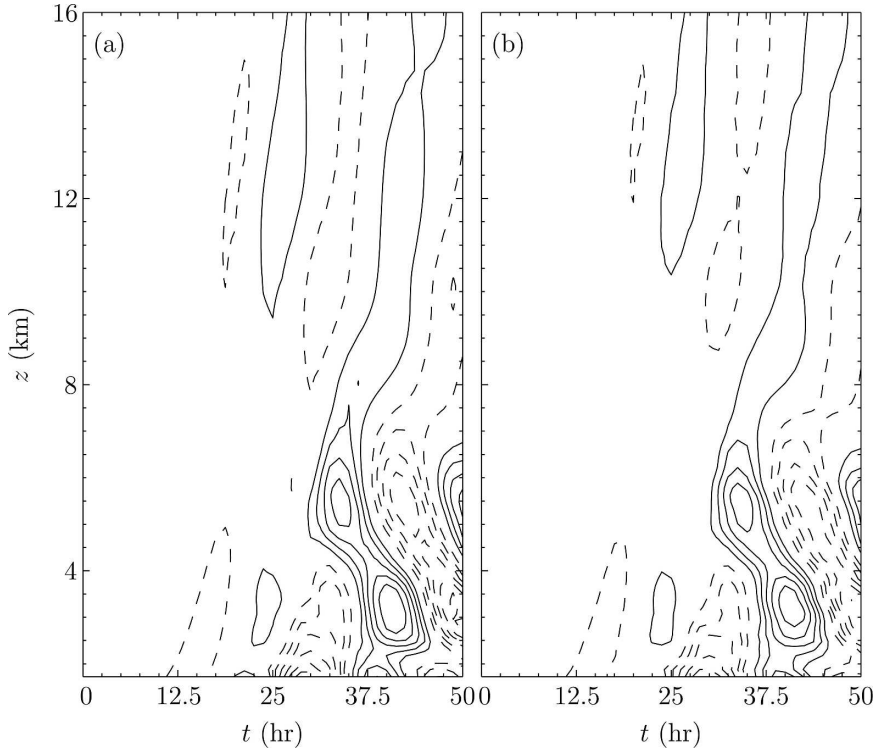

FIG. 16. Time–altitude distribution of $\langle u' \rangle$ (contour interval of 1.5×10^{-2} m s^{-1}) for (a) a simulation with a 1.5-km-high mountain at 6-km horizontal resolution, and (b) a no-mountain, parameterized-GWD simulation at 18-km horizontal resolution.

except that below mountain-top level, the flux divergence is specified as constant with height and equal to the difference between the momentum flux at mountain-top level and the surface pressure drag; F_x and F_y are added to the right side of (1).

In our parameterized-drag simulation, all grid boxes in which the maximum terrain elevation exceeded $h_0/2$ were included in the region over which the total drag force was distributed. (This region is marked by the rectangles in Figs. 18a–d and extends two 18-km grid cells in the x direction and 10 cells in the y direction.) Both w' and the fluxes $\rho_0 u'w'$ and $\rho_0 v'w'$ were very small outside the immediate neighborhood of the mountain, so concentrating these stresses inside the indicated region is consistent with the original simulation that included the actual 1.5-km-high mountain.

The time–altitude dependence of $\langle u \rangle$ for the original simulation of with the 1.5-km mountain on a uniform 6-km mesh is compared in Fig. 16 with the same quantity computed on a uniform 18-km mesh without a mountain in which the preceding GWD parameterization is imposed. Clearly this parameterization does allow one to almost perfectly recover the time and space variations $\langle u \rangle$ that are generated by the actual mountain. This perfection is lost, however, if one examines the spatial structures in u rather that the average over the full horizontal domain.

The zonally averaged u' and q' fields for the no-mountain simulation with parameterized GWD are shown in Fig. 17 for times $t = 20$, 30, 40. and 50 h; these may be compared with the equivalent fields from the original 1.5-km simulation plotted in Fig. 7. There is qualitative similarity between the two cases, including a localized region of deceleration above the ridge, with weaker acceleration farther to the north and south. The GWD parameterization also captures the relatively shallow vertical structure of the perturbations that have been advected well north and south of the mountain. However, except at the final time (50 h), this scheme tends to seriously underestimate the intensity of the flow deceleration over the mountain.[6] For example, this parameterization scheme is unable to produce the dramatic loss of momentum over the mountain at 30 h

[6] Durran (1995) also found that the imposition of perfect momentum flux profiles in a two-dimensional no-mountain simulation produced weaker x-averaged u' perturbations than those in the original simulation containing the mountain from which the fluxes were diagnosed.

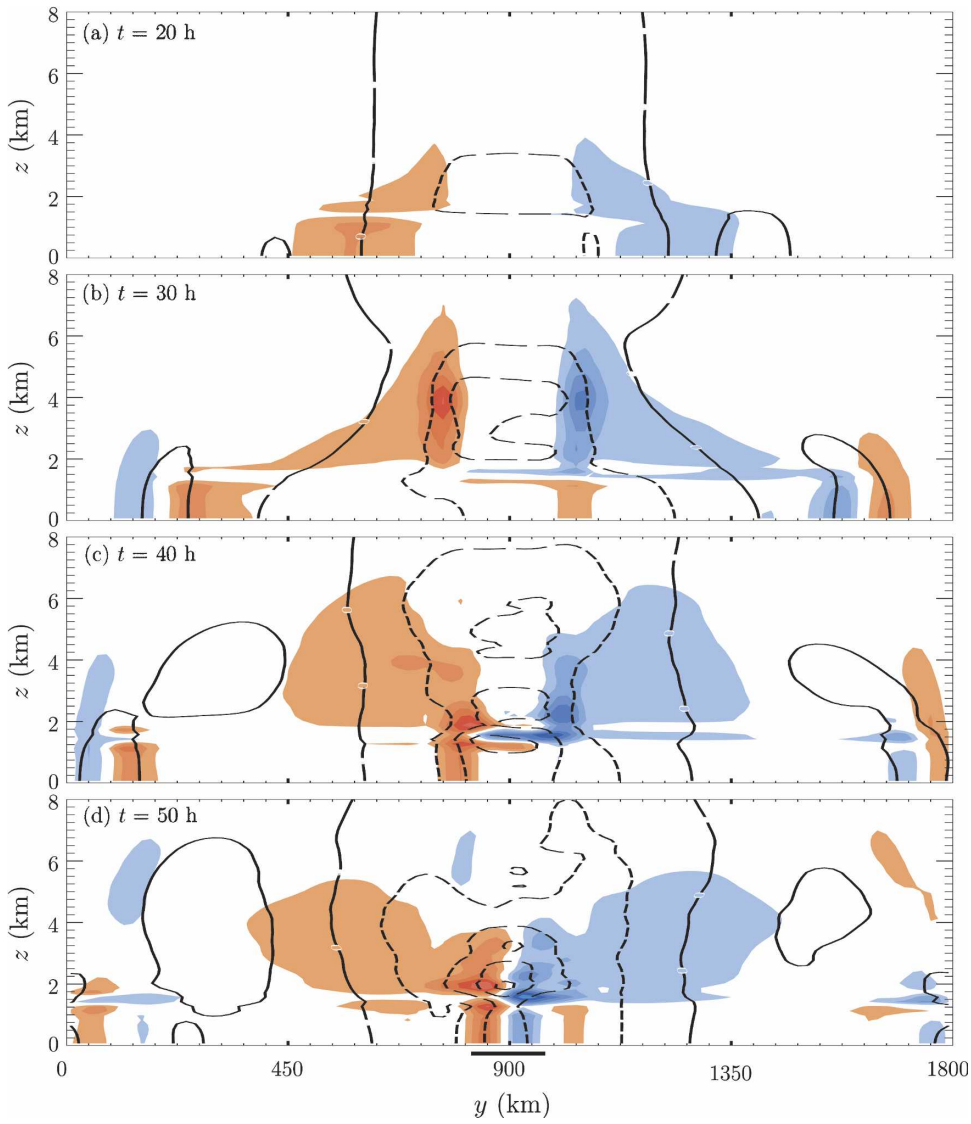

FIG. 17. Same as in Fig. 7, but for the u' obtained using a perfect GWD parameterization. The thick black line along the x axis denotes the region over which the drag force was applied.

found in the true solution (cf. Fig. 17b with 7b) and the PV field is also much weaker.[7]

The spatial structure of the regions of flow acceleration and deceleration at $z = 3$ km in the parameterized-GWD case are plotted in Fig. 18 and may be compared with their equivalents for the $h = 1.5$-km case in Fig. 8. Again there are several qualitative similarities, but the GWD parameterization underestimates the magnitude of the response. Curiously, in contrast to the zonally averaged results, the worst underestimation occurs at $t = 50$ h, where the control simulation with the 1.5-km-high mountain generates u' (and also u'_b) perturbations as strong as -6.1 m s^{-1} near the downstream end of the large-scale jet, while the maximum deceleration in the no-mountain, parameterized GWD case is -1.8 m s^{-1}.

One might suppose that the most difficult challenge for GWD parameterization lies in the estimation of the vertical profiles of momentum flux, since both mountain-wave generation and dissipation can be highly nonlinear processes. Although the correct specification of $\langle \rho_0 u'w' \rangle$ and $\langle \rho_0 u'w' \rangle$ will guarantee the correct evolution of the domain averaged velocity fields, $\langle u \rangle$ and $\langle v \rangle$, as evident in Figs. 17 and 18, this is not enough to guarantee correct reproduction of the strength and

[7] These comparisons hold even if the fields from the control ($h = 1.5$ km) simulation are spatially filtered to the 18-km resolution of the GWD experiment. Since there are still 100 grid intervals in both x and y after such filtering, the momentum fields in the control simulation are virtually unchanged.

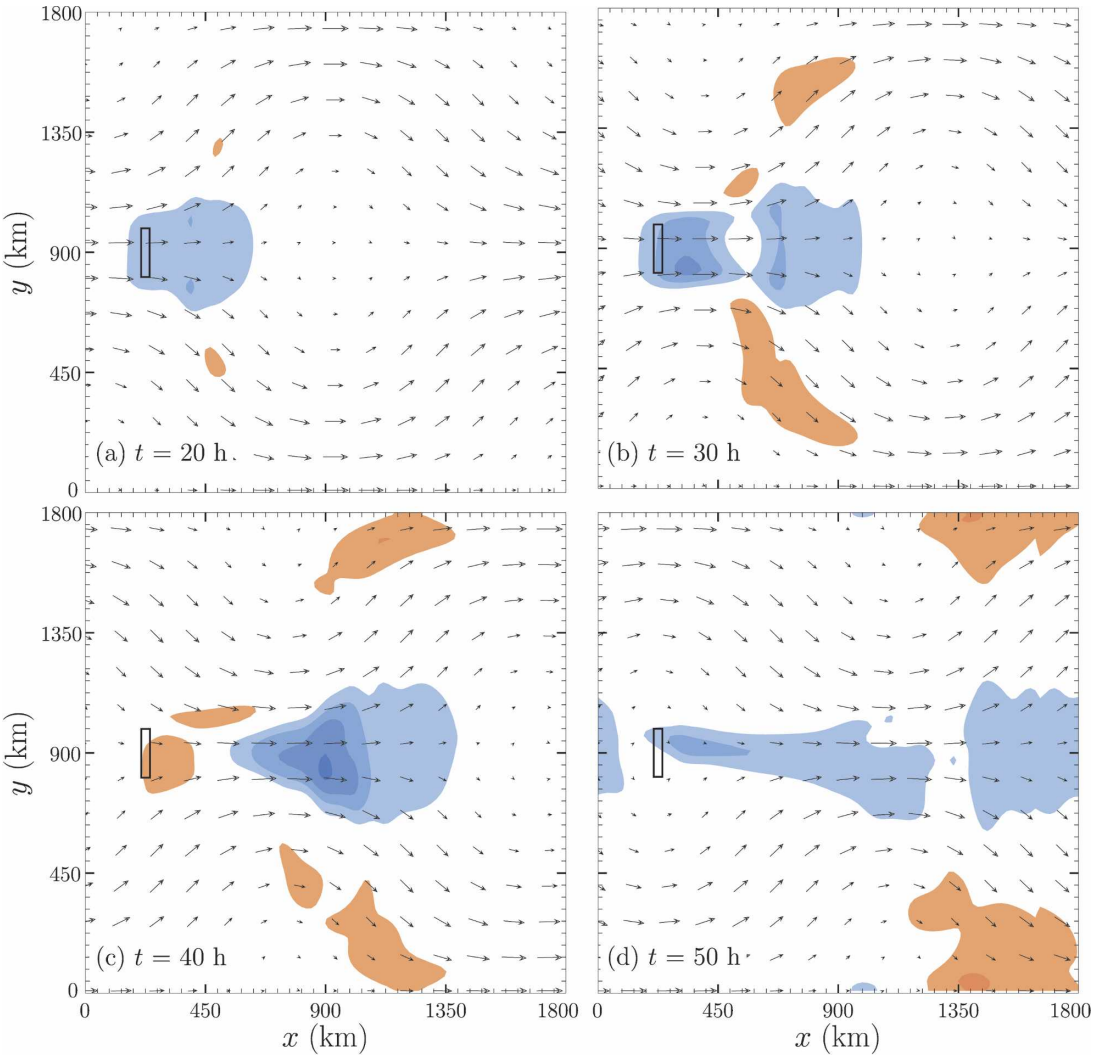

FIG. 18. Same as in Fig. 8, but for the u' obtained using a perfect GWD parameterization. The rectangle indicates the extent of the 20-gridpoint region over which the drag force was applied.

structure of the large-scale response, at least for models with grid spacing on the order of 15–40 km.

As noted in section 5, most of the GWD-induced large-scale velocity perturbations are in geostrophic balance and therefore make no contribution to $\langle u \rangle$ and $\langle v \rangle$. Within the context of our perfect GWD parameterization, PV generation is proportional to the curl of the drag, in particular,

$$\frac{\partial q}{\partial t} + \ldots = \left(\frac{\partial F_y}{\partial x} - \frac{\partial F_x}{\partial y} \right) \frac{\partial \theta}{\partial z} \approx - \frac{\partial F_x}{\partial y} \frac{\partial \theta_r}{\partial z} .$$

The balanced response is therefore sensitive to the spatial distribution of the wave drag, and this distribution is another factor that should be specified in more complete GWD parameterizations. Figure 19 illustrates

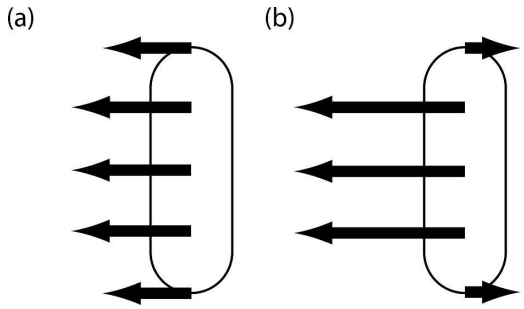

FIG. 19. (a),(b) Possible spatial distributions of GWD forcing producing identical values of $\langle \rho_0 u' w' \rangle$ and $\langle u \rangle$, in which the PV generation, and therefore the strength of the regions of local acceleration and deceleration, are much stronger in (b) than in (a). The arrows indicate (F_x, F_y) vectors with their tails terminating at the centers of five hypothetical grid points located along a poorly resolved isolated ridge.

how different spatial distributions of the drag can generate very different PV anomalies while preserving the same domain-averaged drag. Rather than attempt to estimate the spatial distribution of the drag it may be possible to directly parameterize the generation of PV anomalies, perhaps in connection with an estimate of the Bernoulli-function deficit in the lee of the terrain (Schär and Durran 1997). The formulation of such parameterizations are, however, beyond the scope of this paper.

9. Summary and conclusions

We have examined the impact of transient mountain waves on the momentum and potential vorticity fields in a barotropic, horizontally periodic large-scale flow. Although the strongest features and most important impacts occurred when the mountain was high enough to create breaking waves during almost the entire simulation, even mountains too small to force any wave breaking exerted some influence on the large-scale flow. In the small-amplitude ($h = 250$ m) case, this influence appears to arise from transients in our initial value problem. The time-averaged momentum flux carried through the upper boundary by mountain waves did not come completely into balance with the time-averaged pressure drag during either of the first two 50-h cycles. As a consequence the domain-averaged absolute momentum decreased during each cycle of the large-scale flow, although considerably less absolute momentum was lost during the second cycle. In addition, a region of warm air blows off the mountain when the flow starts to accelerate, and the resulting patch of warm air at the lower boundary appears to induce a cyclonic circulation over the mountain, thereby producing an asymmetric response in which the zonally averaged u' strengthens south of the ridge and weakens to the north.

In the case with a 1.5-km-high mountain, wave breaking occurred throughout most of the simulation and significantly reduced the zonally averaged momentum in a region whose north–south extent was roughly 3 times that of the mountain itself. This central zone of flow deceleration was flanked by zones of weaker mean-flow acceleration farther to the north and south. The differences in the zonally averaged u' field were consistent with the differences in the zonally averaged Ertel potential vorticity field q'.

Except for gravity wave signals near the mountain, the three-dimensional structure of u' was also in approximate geostrophic balance with q'. This was verified by inverting the PV field under the assumption of geostrophic balance. At the end of the cycle ($t = 50$ h) near the level of strongest wave breaking ($z = 3$ km) both u' and u'_b exhibited similar patterns, with flow deceleration in excess of -5 m s^{-1} near the exit of the (initially 20 m s^{-1}) barotropic jet. Regions of acceleration in excess of 2 m s^{-1} were also present north and south of the jet exit region.

Piecewise PV inversion verified that these u' perturbations were associated with a pair of positive and negative PV anomalies generated on the northern and southern flanks of the mountain between hours 25 and 30, which was the period of deepest and most intense wave breaking. After generation, these PV anomalies were advected well downstream of the mountain by the large-scale flow.

Consistent with the fact that the domain integral of the geostrophic velocities is 0 over the periodic domain, and that u' is well approximated by u'_b throughout most of the domain, $\langle u' \rangle$ was much smaller than the extrema in u' itself. As a consequence, gravity wave–drag parameterizations that focus on estimating changes in the mean flow associated with the vertical divergence of $\langle \rho_0 u' w' \rangle$ may fail to properly capture the strength and structure of the large-scale response. This was confirmed by a simulation in which the mountain was removed but the correct z–t dependence of $\langle \rho_0 u' w' \rangle$ and $\langle \rho_0 v' w' \rangle$ was imposed over the region previously occupied by the mountain. Although this "perfect" GWD parameterization yielded the correct values for $\langle u' \rangle$, it underestimated the strength of the extrema in large-scale u' field. The problems with the perfect GWD simulation suggest that future gravity wave–drag parameterization schemes should consider PV-generation properties in addition to global momentum budgets.

Acknowledgments. The authors are indebted to Drs. Chris Davis and Rich Rotunno for helpful discussions. This research was supported by National Science Foundation Grants ATM-0137335, ATM-0228804, and ATM-0506589.

REFERENCES

Chen, C.-C., D. R. Durran, and G. J. Hakim, 2005: Mountain-wave momentum flux in an evolving synoptic-scale flow. *J. Atmos. Sci.,* **62,** 3213–3231.

Durran, D. R., 1995: Do breaking mountain waves decelerate the local mean flow? *J. Atmos. Sci.,* **52,** 4010–4032.

——, 1999: *Numerical Methods for Wave Equations in Geophysical Fluid Dynamics.* Springer-Verlag, 465 pp.

Eliassen, A., and E. Palm, 1960: On the transfer of energy in stationary mountain waves. *Geophys. Publ.,* **22** (3), 1–23.

Epifanio, C. C., and D. R. Durran, 2001: Three-dimensional effects in high-drag-state flows over long ridges. *J. Atmos. Sci.,* **58,** 1051–1065.

——, and ——, 2002a: Lee-vortex formation in free-slip stratified flow over ridges. Part I: Comparison of weakly nonlinear inviscid theory and fully nonlinear viscous simulations. *J. Atmos. Sci.,* **59,** 1153–1165.

——, and ——, 2002b: Lee-vortex formation in free-slip stratified flow over ridges. Part II: Mechanisms of vorticity and PV production in nonlinear viscous wakes. *J. Atmos. Sci.,* **59,** 1166–1181.

Lilly, D. K., 1962: On the numerical simulation of buoyant convection. *Tellus,* **14,** 148–172.

Lott, F., 2003: Large-scale flow response to short gravity waves breaking in a rotating shear flow. *J. Atmos. Sci.,* **60,** 1691–1704.

Queney, P., 1948: The problem of air flow over mountains: A summary of theoretical studies. *Bull. Amer. Meteor. Soc.,* **29,** 16–26.

Rotunno, R., V. Grubsišić, and P. K. Smolarkiewicz, 1999: Vorticity and potential vorticity in mountain wakes. *J. Atmos. Sci.,* **56,** 2796–2810.

Schär, C., 1993: A generalization of Bernoulli's theorem. *J. Atmos. Sci.,* **50,** 1437–1443.

——, and R. Smith, 1993a: Shallow-water flow past isolated topography. Part I: Vorticity production and wake formation. *J. Atmos. Sci.,* **50,** 1373–1400.

——, and ——, 1993b: Shallow-water flow past isolated topography. Part II: Transition to vortex shedding. *J. Atmos. Sci.,* **50,** 1401–1412.

——, and D. R. Durran, 1997: Vortex formation and vortex shedding in continuously stratified flows past isolated topography. *J. Atmos. Sci.,* **54,** 534–554.

Smolarkiweicz, P. K., and R. Rotunno, 1989: Low Froude number flow past three-dimensional obstacles. Part I: Baroclinically generated lee vortices. *J. Atmos. Sci.,* **46,** 1154–1164.